

Paleomagnetic constraints on stratigraphy and rift-related tectonics of Pliocene and Early Pleistocene volcano-sedimentary strata: the Mt. Galili hominid research area, Southern Afar Depression, Ethiopia

Fritz POPP^{1*)} & Robert SCHOLGER²⁾

¹⁾ Department of Geodynamics and Sedimentology, University of Vienna, Althanstrasse 14, 1090 Vienna, Austria;

²⁾ Chair of Applied Geophysics, Montanuniversität Leoben, Peter Tunner Str. 25, 8700 Leoben, Austria;

^{*} Corresponding author, friedrich.popp@univie.ac.at

KEYWORDS Magnetostratigraphy; Plio-Pleistocene volcano-sedimentary deposits; oblique extensional tectonics; East African Rift; Ethiopia

Abstract

Our paleomagnetic investigations in the Northern Main Ethiopian Rift concentrated on ascertaining characteristic remanence directions of volcanic and sedimentary layers embodied within the Mt. Galili Formation (MGF). Magnetic stratigraphy was applied mainly to support anthropological studies on early hominid evolution. The new paleomagnetic results provided implications for stratigraphic age determinations of the MGF, and they also support arguments for rift-related tectonics as block rotation and tilting relative to the stable African crust since the Pliocene.

Based on 497 paleomagnetic samples, we applied magnetic stratigraphy on magmatic and sedimentary rocks to determine the age of the MGF and correlated the results with published ⁴⁰Ar/³⁹Ar age data on tuff and ignimbrite layers which range from ca. 5.4 Ma to ca. 2.3 Ma, consistent with biostratigraphic age constraints. Nine magnetic polarity intervals of the Gilbert zone were identified within the lower four members of the MGF covering a time span from 5.37 to 3.58 Ma. The upper two members of the MGF comprised three polarity intervals assigned to the upper Gauss and lower Matuyama polarity zones. In combination with an ⁴⁰Ar/³⁹Ar age of 2.35 Ma, located in the middle of the section, we infer that ca. 0.5 Ma and four polarity intervals are missing between the MGF's lower and upper members. We attribute this significant depositional gap to uplift of the region due to the intrusion of basalt magma, associated with deposition of the Upper Shabeley Laag Member.

Extensional rift tectonic processes were intimately affiliated with magmatic activity and generation of rapidly changing sedimentary environments of the MGF's deposits, but the bulk of the observed tectonic features resulted from post-depositional tectonic overprint, when the re-orientated Wonji Fault System affected the Mt. Galili area in the Quaternary period, thereby creating new internal rift (in older rift) structures. Tectonic movements of MGF's strata were deduced from our analysed characteristic remanent magnetisation (ChRM) directions compared with Pliocene reference data. The investigation revealed almost unchanged orientation of the ChRM-directions for the marginal internal rift zone in the East of the Mt. Galili area, but moderate counterclockwise rotation for the central internal rift zone in the West. The North of the Mt. Galili area suffered moderate clockwise rotation, probably due to the Mt. Galili area's regional position, adjoining a transfer zone between the Quaternary Angele and Addo-Do magmatic segments.

1. Introduction

The East African Rift in Ethiopia is a well-studied area for its geological and structural development (e.g. Ring, 2014; Corti et al., 2013), and especially as an area of early hominid evolution (e.g. Haile-Selassie et al., 2015; Kimbel and Delezone, 2009; Kullmer et al., 2008; Macchiarelli et al., 2004; Weber et al., 2001; White et al., 1993, 2006, 2009).

The surveyed Mt. Galili (N 9,77°, E 040,55°) area is located in a central sector of the northernmost Main Ethiopian Rift (MER), that propagated north-eastwards into the southern Afar depression during Miocene to Pleistocene times (Hayward and Ebinger, 1996). Thereby, strain patterns changed their directions, and newly generated internal rift fault systems (Wonji faults) replaced marginal rift fault systems (Corti et al., 2013). Thus, Quaternary rift basins and magmatic segments (Fig. 1), which display right-stepping lateral offset-tectonics (Wolfenden et al., 2004; Kidane et al., 2006), formed within Miocene rift basins (Beyene and Abdelsalam, 2005). The lithologic and

tectonic features of the herein described Mt. Galili research area are characteristic of such rift-related settings: The region exposes a fluvial-to-lacustrine sedimentary succession intercalated with volcanic marker beds, and it is extensively faulted by NNE-SSW oriented normal faults combined with trans-tensional movement features. Our new paleomagnetic sites cover a composite profile of the MGF (Fig. 8: d, e) encompassing a ca. 230 meter thick pile of Pliocene to early Pleistocene deposits. Absolute (⁴⁰Ar/³⁹Ar) age data obtained from volcanic tuff layers by Hujer et al. (2015) serve as stratigraphic markers within the examined volcano-sedimentary sequence. Examination of numerous profiles from sedimentary sections (Hujer et al., 2015) and field observations of rift tectonic displacement features were used to determine the stratigraphic positions of the paleomagnetic sample sites.

For the purpose of stratigraphic correlation with other regions of the MER, previous papers have been checked: Earlier

paleomagnetic studies of rift deposits in the Miocene-Pliocene Sagantole Formation (Afar rift region / Middle Awash Valley) revealed eight magnetic polarity zones in the time frame between 5.6 and 3.9 Ma (Renne et al., 1999). Quade et al. (2008) presented a magnetic polarity analysis of deposits of the Southern Afar Rift at Gona for the time span from 6.4 to 0.16 Ma and a magnetostratigraphic study of the eastern Hadar Basin examined the Sidi Hakoma and Denen Dora Members of the Hadar Formation, revealing two normal and one reversed polarity intervals between 3.42 and 3.20 Ma (Dupont-Nivet et al., 2008). Kidane et al. (2009) presented paleomagnetic results from a later rift stage in distinct regions within the MER, linking together volcanic segments of Quaternary age, which yielded about 7° counter-clockwise block rotations along vertical axis. This is consistent with a transtensional deformation process during Quaternary times in the Fentale region (Corti et al., 2013) and is also of relevance for the tectonics in our study area. Erosion and non-deposition affected some areas within the Ethiopian Rift in Quaternary times, which constitutes an important factor in the MGF's stratigraphic record. Recently, Kidane et al. (2014) presented a refined magneto-stratigraphy of the Shungura Formation / Omo Group in SW Ethiopia, unfolding seven polarity zones between 3.60 and 2.32 Ma. The authors suggest evidence for the related Kaena subchron which may have been removed in an erosional episode, leaving a hiatus of at least 70 ka in the Shungura Formation deposits. This feature may relate to the significant upper MGF's sedimentary gap (Fig.8) reported in this study.

2. Geological Setting

The Main Ethiopian Rift (MER) is bound to the northwest by the Ethiopian plateau and to the southeast by the Somalian plateau (e.g. Beyene and Abdelsalam, 2005; Buck, 2006). Both are composed of continental flood basalts of a related magmatism predating continental break-up by several million years (Ayalew et al., 2006). The main tectonic elements of the region, i.e. the Nubian and Somalian plates, suffered initial extension from about 25 Ma ago. Subsequent rifting isolated continental microplates, the Danakil and Ali Sabieh blocks, and the Afar depression started to stretch as these blocks began rotating, what process became dominant since ca. 7 Ma in the Afar region (Audin et al., 2004). Since 11 Ma the northern part of the MER

was already opening out into the stretched Afar depression (Hendrie et al., 1994; Tesfaye et al., 2003; Wolfenden et al., 2004). Generally, the MER opened at a rate of about 2.5 to 5 mm/a in ESE-WNW direction during Miocene to Pliocene times (Wolfenden et al., 2004), whereby large, discontinuous normal border faults developed (Pizzi et al., 2006; Tesfaye et al., 2008). Subsequently, continuous rift extension focused on newly developed magmatic segments of Quaternary age (Ebinger and Casey, 2001; Casey et al., 2006; Keir et al., 2006; Corti, 2009) which were connected with coeval rift basins, interpreted as embryonic oceanic spreading centres (Hayward and Ebinger, 1996; Manighetti et al., 1998; Ebinger and Casey, 2001). The formation and continued expansion of large marginal fault systems induced silicic volcanism, whose felsic volcanic strata capped the flood basalt sequences at first. Over time, the locus of faulting and magmatism migrated in riftward direction, finally forming the Quaternary magmatic segments (Fig. 1) within the MER (Ayalew et al., 2006). Magmatosedimentary deposits of the surveyed MGF formed and suffered tectonic overprinting under this conditions in Pliocene to early Pleistocene times, what is specified in subsequent chapters below.

2.1 Magmatism

In the Pliocene-Pleistocene, an extensive volcanic sequence of the up to 1500 m thick "Afar Stratoid Series", characterized by individual basalt flows, covered about two thirds of the "Afar Fault Embayment" (Varet, 1978). Their unconformable

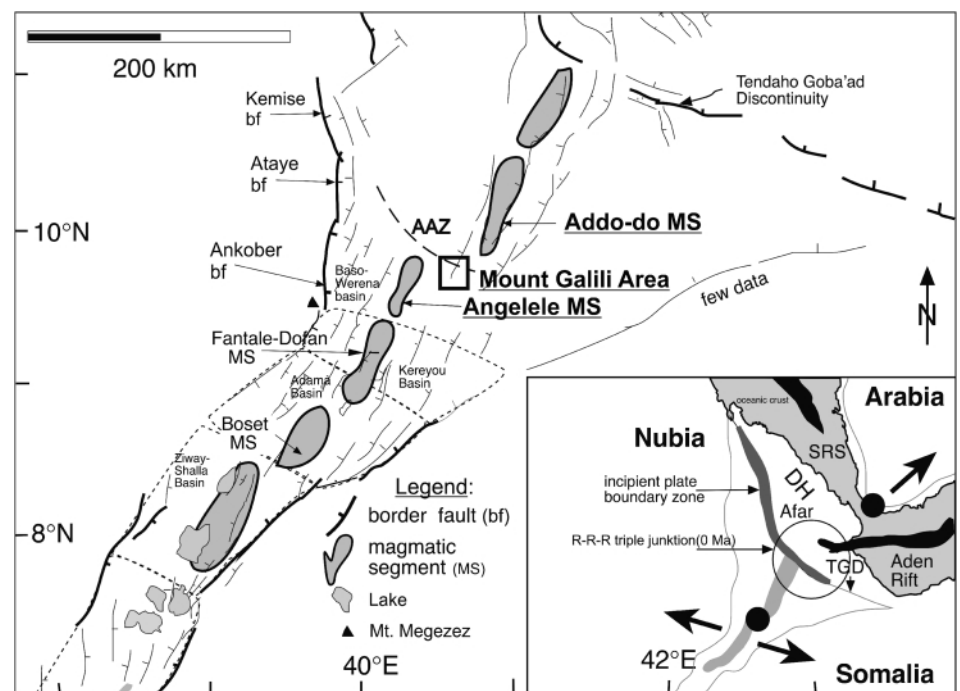
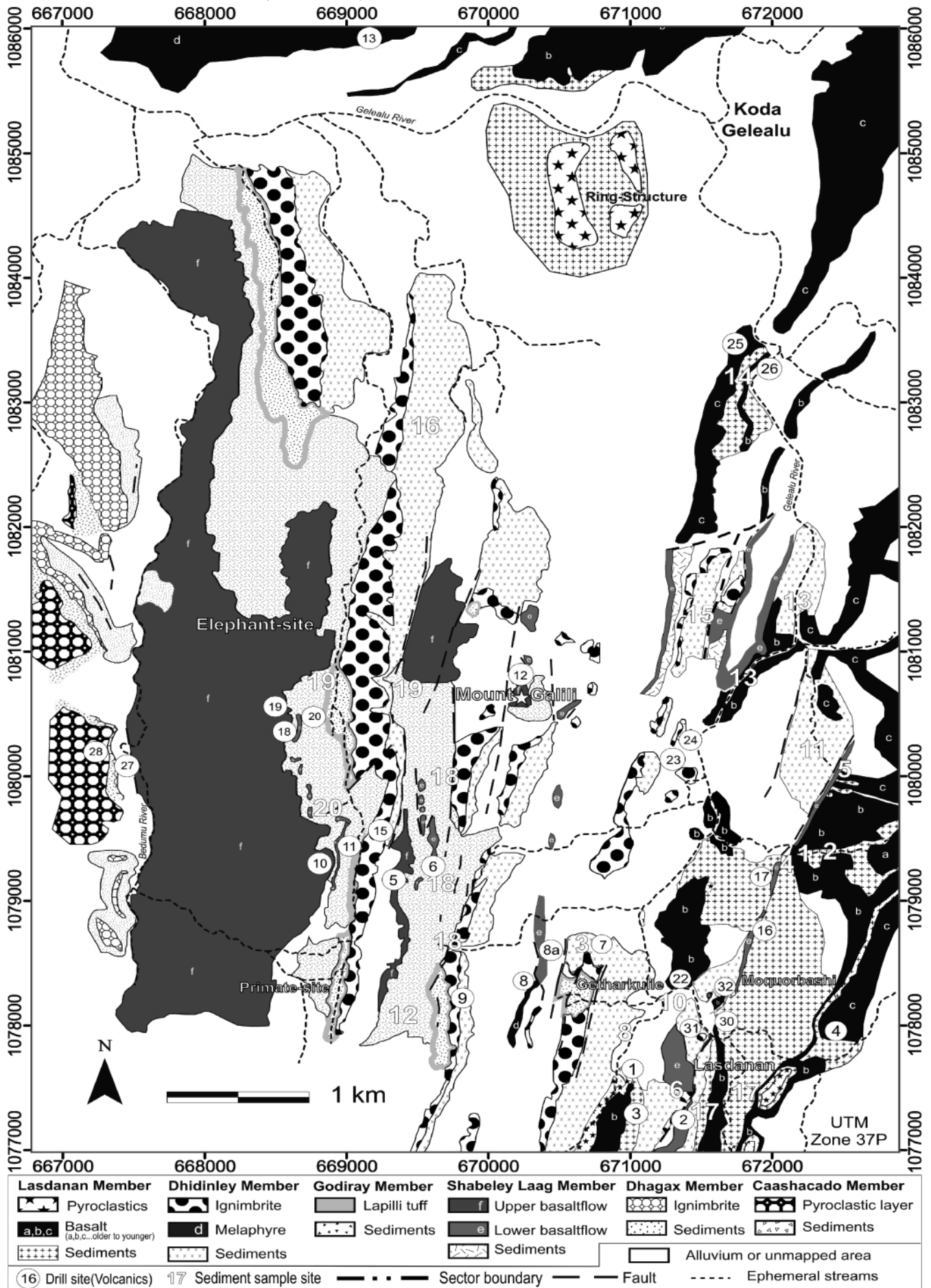


Figure 1: Major faults and along-axis segmentation patterns within the Northern Main Ethiopian Rift (according to Wolfenden et al., 2004). Site of the Mount Galili research area and ambient tectonic patterns are indicated, (AAZ) arcuate accommodation zone. **Inset:** Main features of the MER-Afar Region. (SSR) southern Red Sea, (DH) Danakil horst, (TGD) Tendaho Goba'a discontinuity separating the Red Sea and MER, Arabia and Africa can be reconstructed crudely by overlying black dots, (black arrows) extension directions.



basal contact with the underlying Miocene “Dalha Series” may be due to a period of erosion before the onset of extensive magmatic activity that formed the “Afar Stratoid Series”. Within the contemporaneous MGF, diverse basalt layers show a trend from OIB (ocean island basalt) towards MORB (mid ocean ridge basalt) geochemical signatures, thus highlighting a magmato-tectonic setting between continental and oceanic rifting (Urbanek et al., 2005). Concerning the prominent felsic volcanism, generated from soaring rift faults, Ayalew et al. (2006) reported that the felsic rocks, which erupted during the formation of the MER in the age range from 28 to 2.5 Ma, can be derived from mantle-sourced basaltic magma through fractional crystallization, accompanied by variable amounts of crustal contaminations. Within the MGF, a significant acidic volcanic marker bed (top of the Dhidinley Mb.) features variability from trachytic-, dacitic-, rhyolitic- up to andesitic composition (Urbanek et al., 2005).

According to the stratigraphic concept of the Afar region by Varet (1978) and Beyene and Abdelsalam (2005), there exist ENE-trending, around 4 Ma old volcanic centres, that are intercalated with the “Afar Stratoid Series”. Some of these comprise trachytic and rhyolitic sequences, referred to as silicic centres (Barberi and Varet, 1975, 1977; Varet, 1978), whose impact was dominant in our research area. In this context, the Galili research area contains several basalt fissures, following fault structures that are thought to be intimately connected with widespread pillowed basalt flows as well as with explosive eruptions of silicic magmas, what provided significant stratigraphic marker beds.

2.2 Lithostratigraphy

According to Urbanek et al. (2005) and Hujer et al. (2015), the MGF represents a succession of fluvio-lacustrine sediments, comprising several horizons of volcanic layers, which are subdivided into six members (Figs. 2 and 8: a), each representing a sedimentary cycle and typically ending with strata recording volcanic activity. The volcanic units are regionally assigned to the lower part of the “Afar Stratoid Series” encompassing a time range of ca.4 Ma (Varet, 1978). Sedimentary processes and volcanic activities are intimately coupled with tectonic rifting as well as crustal block-rotation and -tilting. Hence, coeval sedimentation generally shifts from fine-grained lacustrine to coarse-grained fluvial deposits.

2.2.1 Lasdanan Member

Resting on top of a Melaphyr-basalt basement, the Lasdanan Member *sensu* Kullmer et al. (2008) consists of fossiliferous lacustrine mudstones incised by fluvial channels and

intercalated with several porphyric basalt lava flows and tuff horizons. The sedimentary successions are heterogeneous and pinch out laterally, resulting in direct contact of different basalt flows in areas with a lack of primary sediment accumulation. A total of three basalt flows (Fig. 8: d, Bas 1-3), generated from fissure volcanoes could be identified within the sequenced strata of the Lasdanan Member and explosive volcanic surge deposits are intimately connected with their preceding fissure-basalt intrusions.

2.2.2 Dhidinley Member

Overlying the Lasdanan Member, the Dhidinley Member starts with basal coarse-grained, fossiliferous sandstone beds, thereafter overlain by an extended lacustrine sandflat-mudflat deposit enclosing diatomites and a micritic limestone bed. Locally, channel deposits, consisting of well sorted, cross-bedded sandstone are incised into lacustrine strata. Generally, a trend from fine-grained lacustrine deposits with isolated limestone beds to coarse-grained fluvial sands is noticeable. In areas falling dry, mud cracks can be observed and dune sands of probably eolian origin may have developed. This sedimentary succession is capped by a well-developed gray ignimbrite layer (Fig. 8: d, Pyr 1).

2.2.3 Godiray Member

Superposing the distinctive ignimbrite layer of the uppermost Dhidinley Member, the Godiray Member is composed of shale deposits intercalated by layers of pedogenic carbonates and fluvial sands, finally topped with a white, coarse-grained lapilli tuff. Generally, Godiray Member successions hold minor thickness, but definitely represent a discrete sedimentary cycle, that developed in-between successive volcanic airfall deposits.

2.2.4 Shabeley Laag Member

The Shabeley Laag Member consists of a multicoloured, clayey facies with a gastropod limestone bed, followed by fossiliferous cross-bedded sandstone, revealing well-developed point bar structures. These lower units of the Shabeley Laag Member are overlain by a lower Galili basalt flow (Fig. 8: d, Bas 5), that wedges out towards the north and south. The upper units of the Shabeley Laag Member consist of lacustrine and fossiliferous fluvial meandering channel deposits. Finally, this member is capped by the widespread upper Galili basalt flow (Fig. 8: d, Bas6). The general coarsening-upward trend is interpreted to have been controlled by surface uplift due to tectono-magmatic processes. Hence, an erosional surface developed on top of the extensive upper Galili lava flow, which subsequently led to a break of the sedimentary record.

2.2.5 Dhagax Member

A clayey siltstone and sandstone succession of the basal Dhagax Member rests unconformably on top of the upper Galili basalt. Sedimentary features point generally to lacustrine and fluvial environments, but the predominant upper

Figure 2: Geological sketch map of the Mt. Galili research area. Mount Galili Formation (MGF) is subdivided into six members. Basalt layers are labelled (a-g) relative to their stratigraphic position. Paleomagnetic sampling sites are numbered (volcanites encircled, sediments free-standing) and territorial sector division is illustrated as referred to in the text. Map modified after a basic concept of Urbanek et al. (2005). Mount Galili: N 9.771952° E 40.552104°

portion of the Dhagax Member is clearly dominated by volcanic activity, producing a thick pumice tuff and finally ending up in a thin gray to reddish ignimbrite layer (Fig. 8: d, Pyr 2).

2.2.6 Caashacado Member

The Caashacado Member defines the uppermost part of the MGF, comprising lacustrine silt, fluvial sand and a gastropod-bearing limestone layer. The member ends with a thin pyroclastic layer (Fig. 8: d, Pyr 3) on top of the sequence.

2.3 Chronostratigraphy

Urbanek et al. (2005) reported first preliminary radioisotopic ages for an extensively distributed ignimbrite on top of the Dhidinley Member. Later geochronologic investigation by K. Kuiper (Amsterdam) published in Hujer et al. (2015, Tab. 2) provided $^{40}\text{Ar}/^{39}\text{Ar}$ data for this ignimbrite and several other tuff horizons with their full data sets. Eight samples from volcanic air fall tuff and ignimbrite layers comprising the entire MGF, were analysed by means of $^{40}\text{Ar}/^{39}\text{Ar}$ dating of feldspar. These geochronological data are summarized and correlated with our paleomagnetic results in Table 1 and Figure 8. Sample U51 (2.35 ± 0.01 Ma) is a reddish ignimbrite on top of the Dhagax Member. Sample 09/16A (3.87 ± 0.02 Ma) is a whitish, ca.10 cm thick tuff layer of the Shabeley Laag Member, interbedded with sandstone layers. Sample 09/32 is a weathered tuff layer of the Shabeley Laag Member, located within a sedimentary succession below the upper Galili basalt flow. Sample U11 (3.94 ± 0.02 Ma) is an ignimbrite layer from top of the Dhidinley Member, and sample 09-29 (3.97 ± 0.03 Ma) is the basal layer of a lapilli tuff on top of the Godiray Member. Sample 09/16 (4.25 ± 0.02 Ma) is a coarse-grained lapilli tuff, sampled ~22 meters above the base of the Dhidinley Member. Sample W78 (4.43 ± 0.02 Ma) is a whitish tuff from a basal layer of a surge deposit, that locally forms the base of the Dhidinley Member. Sample W133/2 (5.37 ± 0.04 Ma) originates from a ca. 3 m thick, medium-grained, strongly compacted whitish tuff at the base of the Lasdanan Member.

3. Sampling and laboratory methods

In total, 497 oriented drill core and cube samples were taken in the course of this study, both from volcanic strata and sediments.

Several fissure basalt ridges and pillowed basalt layers were sampled. Fissure basalt ridges represent primary feeding channel storages and are closely connected with rift-tectonic structures. Outgassing features increase towards the marginal zones of individual basalt ridges, where they are closely connected with effluent stream textures and acid pyroclastic ejections. Basalt layers represent lava flows extruding from fissures and cones, thereby covering large areas of sedimentary rift deposits. Their basal contact zone often reveals features of fritted argillaceous sediment, when lava effusions sheeted soggy areas of lakes and floodplains. These basalt layers often exhibit concentric weathering features. Basalt samples were collected from six individual lava flows, nestling between sedimentary strata of the MGF.

Airfall volcanic samples were taken from a prominent ignimbrite layer, marking the top of the Dhidinley Member, as well as from distinctive reddish and grey ignimbrite layers of the Dhagax and Caashacado members terminating the MGF. In the case of the most significant acid volcanic marker bed within the Dhidinley Member, Urbanek et al. (2005) identified a variable composition of the volcanic fragments ranging from trachytic to dacitic and rhyolitic source melts at higher alkali levels, whereas at lower alkali content andesitic source melts are suggested. Additionally, sedimentary layers, composed of material such as clay and silty clay, were selected from a composite stratigraphic section, encompassing the entire range of the MGF's deposits (Fig. 8: e).

Mafic lava flows and basalt fissures or felsic pyroclastic flows were sampled with a gasoline-powered drill, and the collected 25 mm-diameter cores were oriented with both, a magnetic and a sun compass. The average difference between sun and magnetic compass readings was 0.1° for all sites, with the highest observed values at drillsites 2 (-6.4°) and 4 ($+7.3^\circ$). Each flow unit was sampled with 7 to 10 cores, spanning the entire exposed thickness of the flow or fissure. Standard 2.2 cm-long specimens were cut from each core for paleomagnetic laboratory analyses. Clay- and silt-layers were sampled using plastic cubes with a volume of 8 cm^3 , each oriented with a magnetic compass.

Specimens were subjected to detailed stepwise demagnetization by means of thermal or alternating field treatment (70° to 670° C and 3 to 140 mT, respectively). During thermal

Sample ID	UTM-East☆	UTM-North☆	Lithology	Stratigraphy	~Age (Ma)	Magnetic Polarity	Polarity Scale★
U51	667371	1080250	Igimbrite	Dhagax Mb	2.35	Reversed	C2r.2r MATUYAMA
09_16a	670971	1079594	Tuff	Shabeley Laag Mb	3.87	Reversed	C2.Ar GILBERT
09_32	668956	1077907	Tuff	Shabeley Laag Mb	3.91	Reversed	C2.Ar GILBERT
U11	669794	1078422	Igimbrite	top Dhidinley Mb	3.94	Reversed	C2.Ar GILBERT
09_29	669010	1082307	Lapilli-Tuff	Godiray Mb	3.97	Reversed	C2.Ar GILBERT
09_16	672366	1080416	Tuff	basal Dhidinley Mb	4.25	Normal	C3n.1n Cochiti
W78	671967	1077428	Tuff	top Lasdanan Mb	4.43	Reversed	C3n.1r GILBERT
W133/2	672626	1079500	Tuff	basal Lasdanan Mb	5.37	Reversed	C3r GILBERT
	☆(Zone 37P)						★(Cande & Kent 1995)

Table 1: Basic Geochronology-sample information and their determined age, merged with magnetic polarity and attributed chronostratigraphy. Samples and age data from Hujer et al. (2015).

demagnetisation, the bulk susceptibility of the specimens was routinely measured to observe possible mineral transformations. Paleomagnetic data analyses included principal component analysis based on visual inspection of orthogonal projections using AGICO Remasoft software (Chadima and Hrouda, 2006). Isothermal remanent magnetisation (IRM) acquisition and back-field experiments, as well as Curie-point determinations of a representative number of the pilot-specimens aided identification of the magnetic mineral content. Accompanying texture measurements by means of anisotropy of magnetic susceptibility were made with the goal of determining the texture. Natural remanent magnetisation was measured on a three-axes squid-magnetometer with an in-line degausser (2G Enterprises). AGICO KLY-2 and MFK-1 instruments were used for measuring low-field magnetic susceptibility and its anisotropy. All measurements were carried out in the Paleomagnetic Laboratory Gams of the Montanuniversity Leoben (Austria).

4. Paleomagnetic results

4.1 Magnetic mineralogy

The intensity and stability of the natural remanent magnetisation (NRM) of the different rock types varied strongly and there was also substantial variability concerning coercivity and unblocking spectra. The sediment samples were characterized by generally low intensities of NRM (median value of all sediments: 0.019 A/m) in comparison with the ignimbrite and mafic rock samples (median value of all volcanites: 2.46 A/m). Acquisition of isothermal remanent magnetisation (IRM) and Curie-point determinations yielded information about the different magnetic mineral associations in the samples. Typically, specimens of Galili basalt and fissure basalt gained remanence at low magnetising fields and were entirely saturated at less than 0.3 T. Contrastingly, airfall volcanic and melaphyre-basalt samples acquired only up to 90% of their saturation IRM at 0.3 T and continued to gain remanence at higher fields, reaching full saturation at field strengths between 0.5 and 1.5 T. The influence of higher coercive minerals was even higher in the sediment samples (Fig. 3).

Most of the temperature dependence of susceptibility determinations of samples from Galili basalt and fissure basalt yielded Curie-point temperatures ranging between 520°C and 585°C, which are indicative of magnetite as the main carrier mineral. Some samples from these two groups showed an additional low-temperature component in the Curie-point curves,

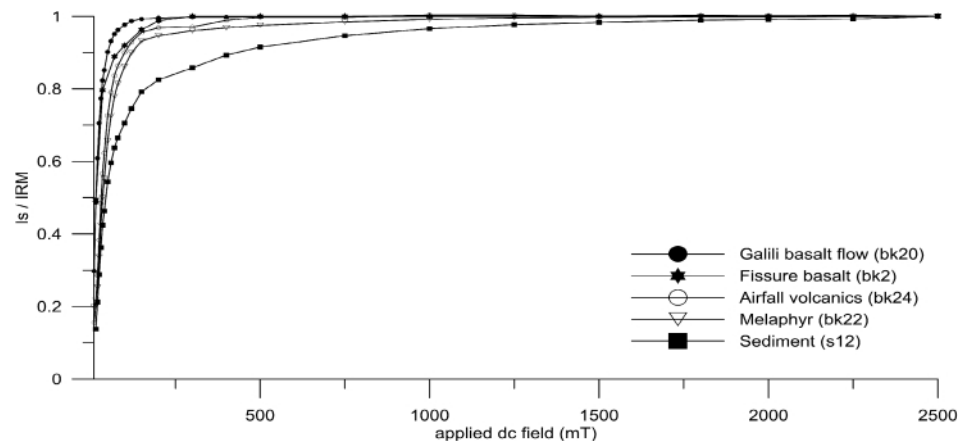


Figure 3: Acquisition of isothermal remanent magnetisation (IRM). I_s/IRM : relative IRM intensity, normalized to IRM acquired at 2.5 T. Two groups could be distinguished within the volcanic rocks: one group showed a rapid increase of intensity already at the first steps of IRM acquisition and full saturation at less than 0.3 T, the second group was characterised by a delayed IRM acquisition, indicating the presence of magnetic minerals with a higher coercivity. The contribution from high-coercive minerals was even higher in the sediment samples.

which we attribute to titanomagnetite. The highest Curie-point temperatures in the range between 620°C and 640°C were observed in airfall volcanites, indicating that maghemite represents the low coercive magnetic phase in these rocks (Fig. 4). Contributions from goethite and hematite could be observed in samples from several basalt flows and sedimentary layers, suggesting these layers were influenced by weathering.

4.2 Alternating field and thermal demagnetization of NRM

Most samples were subjected to progressive alternating field (max 140 mT) demagnetization. Additionally, selected

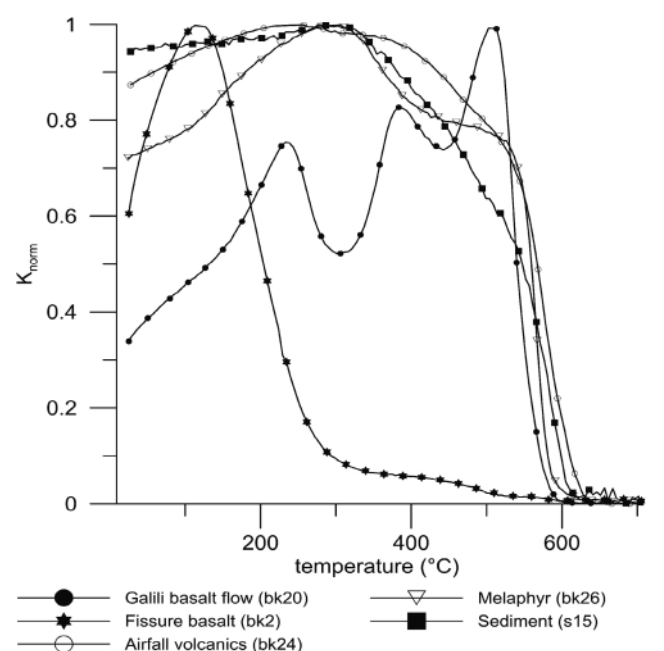


Figure 4: Curie-point determinations for samples from different volcanic and sedimentary rock samples. K_{norm} : volume susceptibility normalized to maximum susceptibility during thermal treatment of each specimen.

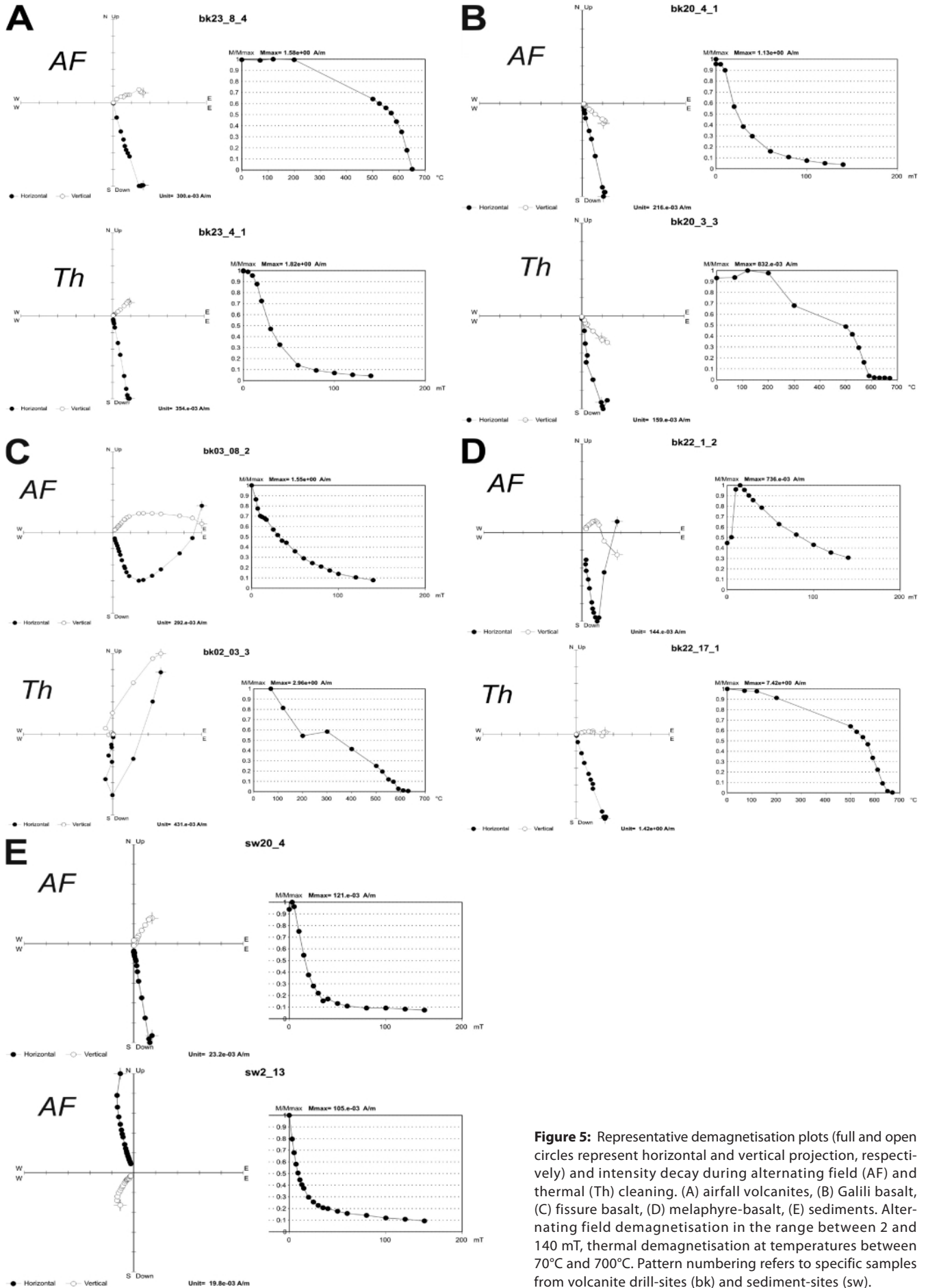


Figure 5: Representative demagnetisation plots (full and open circles represent horizontal and vertical projection, respectively) and intensity decay during alternating field (AF) and thermal (Th) cleaning. (A) airfall volcanites, (B) Galili basalt, (C) fissure basalt, (D) melaphyre-basalt, (E) sediments. Alternating field demagnetisation in the range between 2 and 140 mT, thermal demagnetisation at temperatures between 70°C and 700°C. Pattern numbering refers to specific samples from volcanite drill-sites (bk) and sediment-sites (sw).

samples from each site were thermally demagnetized. In general, the median destructive fields ranged from 5 to 150 mT. For the ignimbrites, it ranged from 25 mT to 40 mT, while basalts showed more variability dependent on the mineral composition. Results from these experiments indicated that magnetite, titanomagnetite and maghemite were the main carriers of the NRM. Higher coercive minerals (hematite and/or goethite) contribute in amounts up to 30% of the NRM. Well defined demagnetisation paths with up to three components of NRM and a good separation of the unblocking temperatures and coercivity spectra could be obtained (Fig. 5).

A viscous component could be removed during the first thermal or alternating field demagnetisation steps of specimens from the pyroclastic material and ignimbrites of the entire study area (airfall volcanites), whereas the second component unblocked at temperatures between 580°C and 640°C and at intermediate alternating field strengths with median destructive fields between 25 mT and 40 mT, indicating maghemite as the main magnetic carrier mineral (Fig. 5 A). This component typically decayed towards the origin and could be regarded as the characteristic remanence direction. With shallow, negative inclinations and mostly southerly declinations, it was indicative of a reversed polarity zone for most of the airfall volcanic materials. An exception is a pyroclastic flow at drillsite 28 (Fig. 2, Tab.2) representing the uppermost stratigraphic position (Fig. 8: d, Pyr 3, Caashacado Mb.) in the MGF, which yields characteristic paleomagnetic directions of normal polarity.

Although there was variability as to the magnetic mineral associations in the samples, similar remanence components were present in specimens from the upper and lower Galili basalt flow. A viscous component could be removed during thermal demagnetisation at temperatures below 200°C or with alternating field-strengths of 5 mT (Fig. 5 B). The remaining components, characterized by low coercivity and unblocking temperatures of 300°C and 580°C, yielded southerly magnetisations with shallow positive (and some negative) inclinations, suggesting a reverse polarity zone for all studied Galili basalt extrusions within the Shabeley Laag Member (Fig. 8: d, Bas 5,6).

Fissure basalt specimens contained two different components of NRM, one of which carried a normal polarity, that was removed at 400°C or 20 mT. Subsequent thermal or alternating field demagnetisation steps yielded a second magnetization vector with a southerly direction and negative inclination, indicating a reversed polarity (Fig. 5 C). Most specimens showed a good separation of the blocking temperatures and coercivity spectra. Similarly, many samples from melaphyre-basalt flows yielded demagnetisation paths containing two antipodal vector components. A low temperature and low coercivity component of normal polarity was typically removed at alternating field strengths below 20 mT and temperatures below 200°C. Subsequently, a well-defined final component with southerly declination and shallow negative inclination could be observed by means of both demagnetisation me-

thods (Fig. 5 D). The final component with unblocking temperatures between 580°C and 640°C and comparably high coercivity (up to 100 mT median destructive fields) was regarded as the characteristic remanence direction.

The quality of the demagnetisation data from sedimentary layers differed substantially from those presented above. The clay specimens of the MGF were characterised by generally lower susceptibilities and lower intensities of NRM. IRM-acquisition (Fig. 3) and Curie-point determinations (Fig. 4) gave evidence for a significantly different magnetic mineralogy. With an unblocking temperature higher than 600°C, evidently hematite contributed considerably to the high-coercivity spectra. During thermal demagnetisation, mineral transformations occurred at higher temperatures in most of the specimens. During alternating field demagnetisation specimens rapidly lost remanence at low demagnetising field strengths, but none of the specimens was entirely demagnetised at 140 mT (Fig. 5 E). However, well grouped vector components of different polarity were observed predominantly in sediment samples that were affected by thermal overprint from volcanic flows. We interpreted this component as the characteristic remanent magnetisation acquired during the cooling of the lava flows/ignimbrite eruption and sedimentation/diagenesis of clay/silt layers, respectively.

4.3 Characteristic remanence directions

Characteristic remanent magnetisation directions (ChRM) for single samples were determined by principle component analyses of the magnetisation components observed during thermal or alternating-field demagnetisation using Remasoft 3.0 software (Chadima and Hroudá, 2006). The quality of the demagnetisation data varied strongly in accordance with the different rock types. More than 70 percent of the samples (354 out of 497) yielded interpretable demagnetisation patterns. The directions of the primary components, which were used for the magneto-stratigraphic zonation and tectonic interpretation, are presented in stereographic projections in Figure 6. Mean values and statistical parameters are presented in Table 2.

The pyroclastics and ignimbrites (Fig. 6 A, airfall volcanics) yielded well-grouped remanence vectors with southerly mean directions indicating reverse polarity except an ignimbrite sample (bk 28) from Drill Site 28 (Fig. 2, Tab. 2), representing the uppermost stratigraphic position in the MGF (Fig. 8: d, Pyr 3, Caashacado Mb.). All site-mean directions of the Galili basalt gave southerly declinations indicating reverse polarity again (Fig. 6 B). However, the mean inclinations of all but one sample (bk 18_19) of this rock type were shallow positive, which is not in agreement with the paleogeographic position. The nature of the deflecting inclinations is yet unclear, but the effect of secular variation of the Earth's magnetic field may be a possible explanation. The main group of fissure basalt samples, originating from the eastern sector of the Galili research area yielded well grouped southerly site mean directions indicating reverse polarity. In contrast, one basalt sample

Sample Site	Locality	Strat.Pos.	Lithology [*]	UTM-East	UTM-North	n	D.b.c.	I.b.c.	k	α 95	D.a.c.	I.a.c.	k	α 95	Rot	Inc diff	Tub	LT trans.	Kbulk
Airfall volcanics																			
Drillsite 28	W area	Pyr 3	Pyroclastics	667270	1080029	19	6.7	28.6	198.8	2.4	5.1	31.5	199.9	2.4	2	19	630		0.009860
Drillsite 27	W area	Pyr 2	Pyroclastics	667270	1080029	9	174.3	-14.8	213.6	3.5	171.4	-17.1	216.7	3.5	-12	-4	580		0.019900
Drillsite 9	W area	Pyr 1	Ignimbrite	669569	1078347	11	171.9	-10	241.2	2.9	171.9	-10	241.2	2.9	-11	3	630		0.022300
Drillsite 15	W area	Pyr 1	Ignimbrite	669269	1079551	12	168.1	-10.8	72.2	5.1	168.1	-10.8	72.2	5.1	-15	2	580		0.014900
Drillsite 7	SE area	Pyr 1	Ignimbrite	670666	1078562	8	169.3	-7.2	142.5	4.7	169.3	-7.2	142.5	4.7	-14	6	640		0.014500
Drillsite 23	SE area	Pyr 1	Ignimbrite	671219	1080047	11	164.9	-9.2	146.1	3.8	165.3	-24.2	146.6	3.8	-18	-11	640		0.008200
Drillsite 24	SE area	Pyr 1	Ignimbrite	671328	1080158	9	172.5	-21.9	247.4	3.3	169.4	-14.3	245.6	3.3	-14	-1	640		0.014400
Drillsite 31	SE area	Pyr 1	Ignimbrite	671470	1077958	4	172.8	-1.1	123.6	8.3	181.1	-29.2	123.1	8.3	-2	-16	n.c.		0.013217
Galili basalt flow																			
Drillsite 12	W area	Bas 6	Basalt [f]	670228	1080817	13	167.9	36	31.1	7.6	167.9	36	31.1	7.6	-15	49	570	-120	0.021000
Drillsite 5	W area	Bas 6	Basalt [f]	669415	1078601	5	185.5	34.1	411	3.8	185.5	34.1	411	3.8	3	47	300	-130	0.004940
Drillsite 10	W area	Bas 6	Basalt [f]	668897	1079295	11	175.1	7.1	128	4.1	175.1	7.1	128	4.1	-8	20	550	-130	0.008500
Drillsite 18+19	W area	Bas 6	Basalt [f]	668475	1080366	10	175.2	-23.1	100.8	4.8	172.3	-17.2	100.8	4.8	-11	-4	670		0.015100
Drillsite 20	W area	Bas 5	Basalt [e]	668584	1080477	10	171.8	11.8	277.6	2.9	174	17.9	276.7	2.9	-9	31	580		0.005740
Drillsite 6	W area	Bas 5	Basalt [e]	669469	1078955	7	166.8	12.4	297.8	3.5	166.8	12.4	297.8	3.5	-16	25	550	-90	0.008820
Drillsite 11	W area	Bas 5	Basalt [e]	668919	1079296	14	174.4	1.5	135.5	3.4	174.4	1.5	135.5	3.4	-9	15	550	-140	0.005780
Drillsite 8a	SE area	Bas 5	Basalt [e]	670382	1078484	6	164.1	16.9	124.6	6	164.1	16.9	124.6	6	-19	30	580	-90	0.005260
Fissure basalt																			
Drillsite 2	SE area	Bas 5	Basalt [e]	671342	1077227	7	169.8	-12.3	39.1	9.8	169.8	-12.3	39.1	9.8	-13	1	580	-160	0.019800
Drillsite 13	W area	Bas 4	Basalt [d]	668834	1085776	9	9.7	-2.7	24.4	10.6	9.7	-2.7	24.4	10.6	7	-16	570	-130	0.020400
Drillsite 4	SE area	Bas 3	Basalt [c]	672578	1077996	8	182.5	-12	34.9	9.5	182.5	-12	34.9	9.5	-1	1	580	-170	0.013500
Drillsite 25	NE area	Bas 3	Basalt [c]	671707	1083312	6	189.3	0.3	55.5	9.1	189.6	2.4	55.5	9.1	7	15	530		0.021600
Drillsite 3	SE area	Bas 2	Basalt [b]	670892	1077137	7	176	-12	46.4	9	176	-12	46.4	9	-7	1	530	-180	0.042700
Drillsite 14	Satkawini	Bas 1	Basalt [a]	675894	1086838	5	147.5	-17.8	43.6	11.7	147.5	-17.8	43.6	11.7	-36	-5	570	-180	0.009940
Melaphyr flows and relatives																			
Drillsite 16	SE area	Bas 5	Basalt Dyke [e]	671774	1078612	5	189.6	-42.3	29.8	14.3	189.6	-42.3	29.8	14.3	7	-29	630		0.014200
Drillsite 8	SE area	Bas 4	Melaphyrbasalt [d]	670294	1078373	8	355.5	30.5	366.6	2.9	355.5	30.5	366.6	2.9	-8	18	640	-60	0.012700
Drillsite 1	SE area	Bas 2	Rhyolite [b]	670924	1077513	7	173.1	-14.3	344.8	3.3	170.2	-10.3	344.8	3.3	-13	3	630	-190	0.008800
Drillsite 22	SE area	Bas 2	Melaphyrbasalt [b]	671228	1078167	20	170.9	-6	81.6	3.6	170.3	-1.1	81.6	3.6	-13	12	640		0.017600
Drillsite 32	SE area	Bas 2	Melaphyrbasalt [b]	671590	1078224	5	171.7	-10.6	355.8	4.1	170.2	-7.3	355.8	4.1	-13	6	n.c.		0.020755
Drillsite 26	NE area	Bas 2	Melaphyrbasalt [b]	671831	1083292	10	197.1	-6.4	113.9	4.5	196.2	-4.1	113.9	4.5	13	9	630		0.008580
Drillsite 21	Satkawini	Bas 1	Melaphyrbasalt [a]	675823	1087024	12	136.7	-30.9	119.8	4	130.7	-22	119.8	4	-52	-9	630		0.016300
Sediments (A=Lasdanan Mb, B=Dhadinley Mb, C=Godiray Mb, D=Shabeley Laag Mb, E=Dhagax Mb)																			
SedSITE 20	W area	D	Clay	668741	1079660	4	173.8	-19.1	92.55	9.6	166.8	-19.2	92.6	9.6	-16	-6	n.c.		0.003545
SedSITE 18	W area	B - D	Clay	669575	1079785	6	158.2	-22	30.1	12.4	151.7	-18	26.2	13.3	-31	-5	550		0.002535
SedSITE 16	W area	B	Clay	669487	1082229	6	342.8	9.1	72.2	7.9	342.1	8.6	27.7	13	-21	-4	n.c.		0.001315
SedSITE 13	NE area	D	Clay	672112	1081511	6	351.1	14.8	64.6	8.4	352.4	3.5	40.4	10.7	-11	-10	n.c.		0.000631
SedSITE 15	NE area	B - D	Clay	671706	1081587	9	358.3	5.1	20.6	11.6	357.6	10.3	18.7	12.2	-5	-3	600		0.006947
SedSITE 14	NE area	A	Clay	671720	1083135	5	358.6	7.7	11.4	23.6	357.4	0.4	12.4	22.6	-6	-13	n.c.		0.003694
SedSITE 3+19	SE+W area	B - C	Clay	668902	1080468	6	175.4	-11.3	39.7	10.8	174.7	-9.5	39.7	10.8	-8	4	550		0.001118
SedSITE 5	SE area	B	Clay	672459	1080064	9	347.6	28.6	20.3	11.7	350.3	18.4	21.6	11.3	-13	5	n.c.		0.003083
SedSITE 2+4	SE area	A	Clay	672013	1079122	14	351.7	20.4	72.2	4.7	350.9	20.5	61.9	5.1	-12	8	n.c.		0.004111
SedSITE 11	SE area	A - B	Clay	672306	1079986	9	346.4	10.6	16.6	13	346.2	7.7	28.6	10.5	-17	-5	600		0.001360
SedSITE 17	SE area	A - B	Clay	671474	1077239	9	354.9	23.3	48.2	7.5	350.7	22.6	39.4	8.3	-12	10	n.c.		0.002547
Overall mean direction incl. NE extended research area:																			
Overall mean direction Galili area s.str.:																			
Mean direction without Galili basalt:																			
9.6, 13.3, 13, 10.7, 12.2, 12.2, 10.8, 11.3, 5.1, 10.5, 8.3, 9.6, 18, 5.4, 23, 30, 4.7																			

[*] Basalt numerated as shown in Fig.8(b)

Table 2: Paleomagnetic data for the Mt. Galili research area. Sample site locality as indicated in Fig. 2. Stratigraphic position as shown in Fig. 8 a,d. (n) number of samples used to calculate the mean vector component, (D b.c. and I b.c.) site mean declination and inclination before tectonic correction, (D a.c. and I a.c.) declination and inclination after tectonic correction, (α 95 and k) are the statistical parameters of a Fisherian distribution, (Rot) difference between the bedding corrected site mean declination and the 5Ma reference direction ($5^\circ/13^\circ$); positive values for clockwise, negative values for counterclockwise rotation. (Inc diff) difference between the bedding corrected site mean inclination and the 5Ma reference direction ($5^\circ/13^\circ$), (Tub) maximum unblocking temperature in $^\circ\text{C}$, (MDF) median destructive field, (TC) Curie-temperature in $^\circ\text{C}$, (LT trans) low temperature transition in $^\circ\text{C}$, (Kbulk) mean volume susceptibility in SI-units. Sample site localities are shown in Fig. 2; UTM data give their geographic position; stratigraphic position and lithology of samples are indicated as shown in Fig. 8 a-e.

(bk 13) from the outermost North of the Galili research area (Fig. 2: drillsite13) showed normal polarity and a single basalt sample (bk 14) from Satkawini, located further to the NE from the research area (drillsite14) displayed significantly larger amounts of counterclockwise rotation (Fig. 6 C). The melaphyre-basalt and related flows revealed a comparably large scatter of the site mean directions and variable α_{95} -values (Fig. 6 D). The mean directions pointed towards reverse polarity except for a single melaphyre-basalt sample (bk8) from drillsite 8 (Fig. 2), which is presumed to be an isochronous volcanic event with basalt flows from drillsite 13 mentioned above. The mean direction of a strongly tilted melaphyre-basalt (bk 30) from drillsite 30, located in the SE sector (Fig. 2) yielded irregular data before tilt correction, but becomes shallow negative after tilt correction with respect to the internal layering of the basalt pillows, indicating that the remanence was acquired before tilting. There was no geological evidence for the tilting of sample bk16 from a basalt dyke located in the SE sector (Fig. 2: drillsite 16), but the irregular steep direction of the mean vector let us suggest, that a tilt correction would be required. The paleomagnetic results for the sediments were of variable quality in accordance with the magnetic mineral composition. In general, the site mean directions were reasonably well grouped, both polarities occurred, and the remanence vectors showed counterclockwise rotation (Fig. 6 E).

5. Discussion

5.1 Discussion and interpretation of paleomagnetic results

Volcanic drill core samples from various stratigraphic levels (Fig. 8: d) and sediment cube samples combined from several outcrops, but correlated with specific members of the MGF (Fig. 8: e) were used to analyse their characteristic remanence directions and magnetic polarity in order to enable correlation with the global paleomagnetic polarity time scale (GPTS) of Cande and Kent (1995). The correction with field data allowed an approximate valuation of post-depositional tectonic rotation and tilting of the MGF's strata (Fig. 7a). Characteristic magnetic vector intensities, orientation and assigned magnetic polarity for particular sediment samples together with their geographic position are given in Table 3. Verification of our new paleomagnetic data is based on the expected paleodirection of the Earth's magnetic field in early Pliocene times and their correlation with the GPTS, supported by absolute age data of several airfall volcanic marker levels.

Figure 6: Site mean directions with α_{95} confidence circles before (left) and after (right) tilt correction. Equal area projection displayed with solid symbols for lower hemisphere and outlined symbols for upper hemisphere. (A) airfallvolcanites, (B) Galili basalt, (C) fissure basalt, (D) melaphyre-basalt (E) sediments. Lithologic grouping, stratigraphic position and statistical parameters as presented in Tab.2. (bk) drill core specimens.

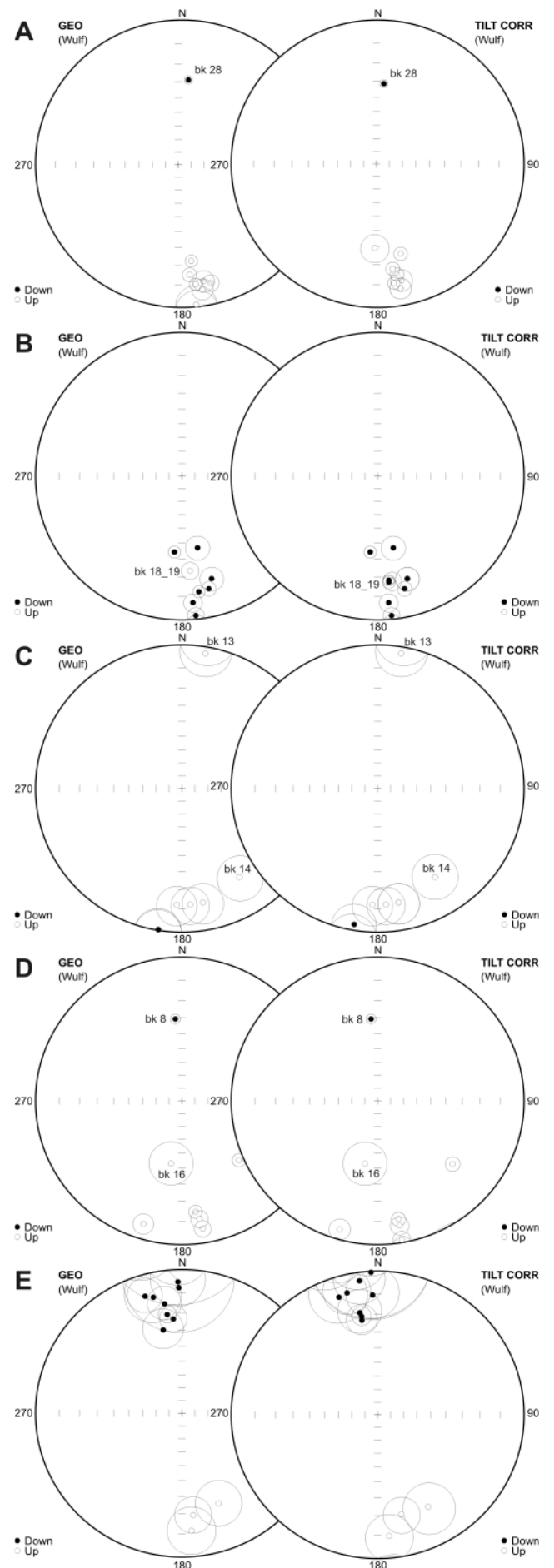


Table 3: Magnetic polarity, magnetic vector orientation and ChRM-vector intensity of sediment samples from various sites ("Sed Sites") of the research area as indicated in Fig. 2. UTM gives the geographic position of individual samples. For stratigraphic range of the "SedSite"-profiles see Fig. 8: e. ChRM intensity data (M[a/m]) derived from alternating field demagnetisation in the range of 2 to 140 mT.

According to the reference curve from Besse and Courtillot (2003), the expected paleodirection for the mean latitude and longitude of the study area at an age of 5 Ma has a declination of 3° and an inclination of 13°. The Earth magnetic field direction during the sampling period 2008 had a declination of 1.6° and an inclination of 3.9° according to the International Geomagnetic Reference Field (Thébault et al., 2015). Concerning our major study area (Mt. Galili area s.str.), a total of 34 sites yielded an overall mean direction of 352.5° / 9.4° with an α_{95} of 5.5° before tilt correction and 351.3° / 8.1° with an α_{95} of 5.3° after tilt correction. The suspicious vector directions of the majority of the Galili basalt samples (Fig. 8: d, Bas 6, Shabeley Laag Mb.) holding southerly declinations and positive inclinations indicated, that the characteristic remanence vectors found in these basalt samples were not representing primary remanence directions. After exclusion of all data of the Galili basalt (8 sites), the remaining 32 sites gave an overall mean direction of 352.9° / 14.9° with an α_{95} of 4.7° before and 351.4° / 13.2° with an α_{95} of 4.7° after tilt correction (Tab. 2). The mean tilt-corrected inclination value of the reduced dataset fits with the expected paleoinclination, whereas the counterclockwise deflecting overall mean declination gave evidence for trans-tensional tectonic dis-

Polarity of primary Vectors from Sediment-Samples:

Sample No	Polarity	Dec	Inc	M[A/m]	GPS-Nr	Zone	UTM-East	UTM-North
SedSite 1: Morquorbashi North, Sediments below Basalt Flow (SE Sector)								
1-2	N	7.8	3.8	2.79E-02	3	37P	672256	1079437
1-4	R	140.3	6.4	4.21E-04	3	37P	672256	1079437
1-7	N	351.4	-0.3	8.28E-02	3	37P	672256	1079437
SedSite 2: Morquorbashi North, fritted Sediments below Basalt Flow (SE Sector)								
2-7	N	25.1	25.3	3.05E-01	6	37P	672405	1079427
SedSite 3: Get Hercule West (SE Sector)								
3-2	N	356.4	13.1	8.13E-03	9	37P	670576	1078446
3-3	N	348.5	18.1	2.27E-03	10	37P	670537	1078467
3-6	R	166.2	-30.5	3.05E-03	126	37P	670774	1078455
3-7	R	185.0	-2.5	1.09E-03	127	37P	670597	1078620
3-8	R	171.7	-8.7	7.09E-03	128	37P	670588	1078480
SedSite 4: Morquorbashi North, Las Danan Sediments (SE Sector)								
4-4	N	357.6	17.2	2.36E-02	13	37P	672016	1079125
4-6	N	355.0	14.8	9.29E-04	55	37P	672077	1079194
SedSite 5: Mealphyr Area E from Strike Slip Basin (SE Sector)								
5-3	N	5.9	33.6	3.24E-04	56	37P	672454	1080061
5-4	N	1.0	24.3	1.59E-03	57	37P	672579	1080036
5-5	N	347.3	21.2	6.13E-02	58	37P	672465	1079976
5-9	N	309.6	49.7	5.10E-02	59	37P	672404	1079979
SedSite 6: Las Danan Area West (SE Sector)								
6-1	R	163.0	-5.4	2.70E-02	20	37P	671263	1077416
SedSite 7: Satkawini (not shown on map)								
7-1	N	358.0	13.2	1.85E-02	26	37P	675554	1087193
7_2	N	6.1	-30.9	3.55E-04	27	37P	675440	1087212
7-3	R	171.7	-30.2	1.96E-03	28	37P	675228	1087178
SedSite 8: Gele Alu River South (SE Sector)								
8-2	N	355.3	9.5	8.72E-03	31	37P	670966	1077917
8-4	R	172.7	-6.2	7.31E-04	125	37P	670950	1078171
SedSite 10: Gele Alu River South, stream bifurcation(SE Sector)								
10-2	R	162.8	-16.7	8.38E-04	34	37P	671189	1078167
10-6	R	173.5	-0.7	5.03E-04		37P	671189	1078167
SedSite 11: Strike-Slip-Basin (SE Sector)								
11-3	N	355.0	3.4	9.19E-04	52	37P	672267	1079850
11-4	R	166.0	-2.4	2.79E-03	50	37P	672317	1080118
11-5	R	166.0	8.8	2.87E-03	60	37P	672310	1079980
11-6	R	173.6	-14.3	5.67E-04	120	37P	672275	1080084
11-7	R	154.5	-14.1	5.07E-03	121	37P	672251	1080059
11-8	N	0.2	14.0	1.62E-03	122	37P	672239	1079992
11-10	R	173.6	-32.2	1.13E-03	124	37P	672214	1079928
11-11	N	349.7	12.6	9.78E-03	129	37P	672251	1080684
SedSite 12: Shabeley Laag Mb N from Camp (W Sector)								
12-1	R	166.9	-13.5	5.90E-04	64	37P	669239	1078076
12-2	R	174.6	-2.6	8.26E-04	64	37P	669239	1078076
12-5	R	151.6	-4.2	5.52E-04	64	37P	669239	1078076
12-6	R	166.9	14.7	1.14E-03	64	37P	669239	1078076
12-7	R	178.8	-6.5	4.83E-03	64	37P	669239	1078076
SedSite 13: Melaphyr Area, middle Gele Alu Riverbed (SE Sector)								
13-1	R	198.7	-1.8	1.09E-02	66	37P	671853	1080969
13-2	N	341.1	14.3	1.24E-02	65	37P	671670	1080775
13-3	N	6.7	14.6	7.61E-03	68	37P	672075	1081358
13-6	N	351.3	14.8	6.86E-03	71	37P	672126	1081602

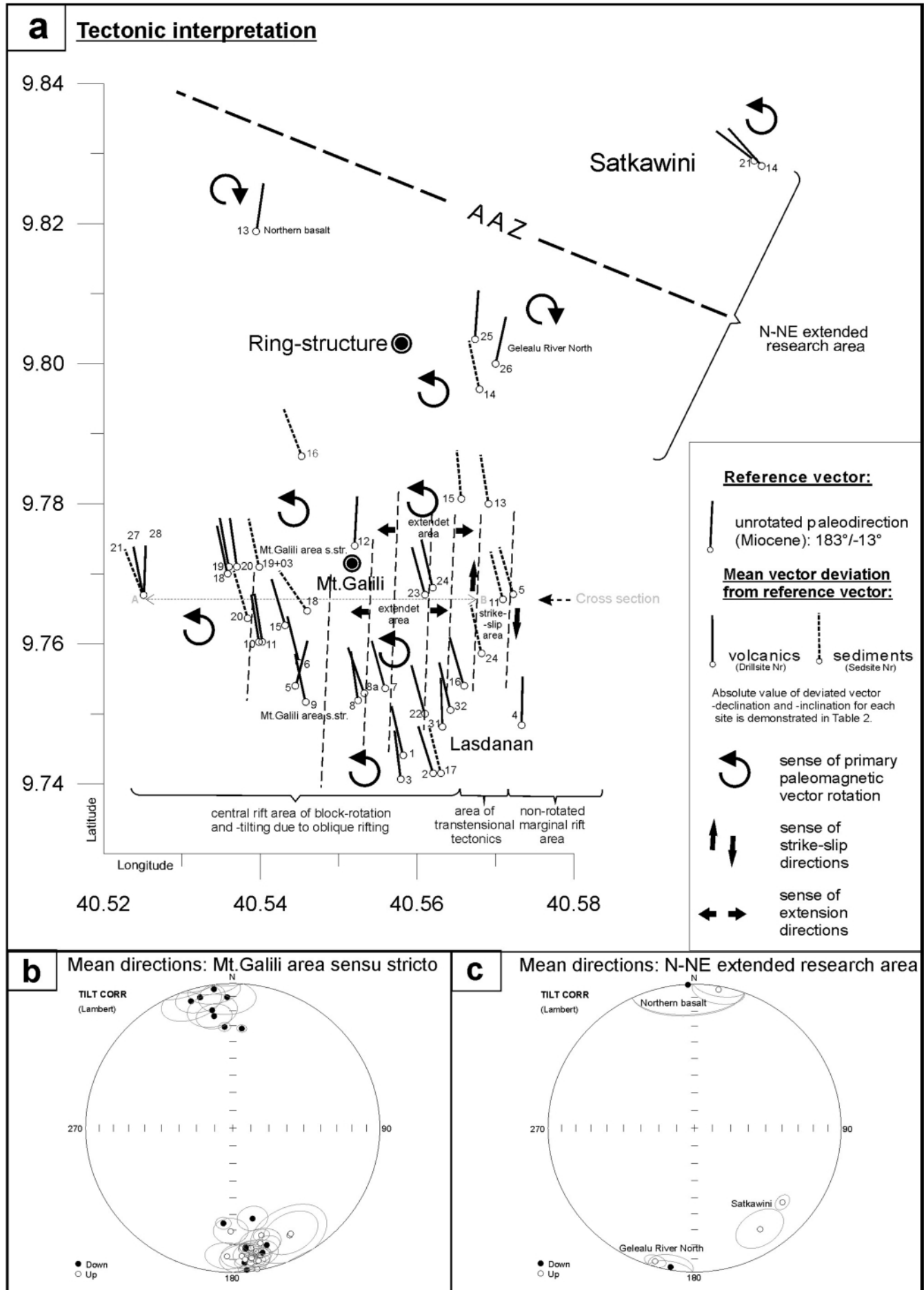
Sample No	Polarity	Dec	Inc	M[A/m]	GPS-Nr	Zone	UTM-East	UTM-North
SedSite 14: Northern Gele Alu Riverbed (NE Sector)								
14-5	N	349.2	19.4	6.17E-02	73	37P	671720	1083133
14-6	R	194.6	16.7	1.44E-01	73	37P	671720	1083133
14-7	N	1.1	19.7	2.10E-02	74	37P	671683	1083115
14-8	R	190.7	8.6	1.79E-03	75	37P	671776	1083238
SedSite 15: Extensional basin E from Mt Galili (NE Sector)								
15-1	R	186.8	-11.1	5.48E-02	konstruiert	37P	671650	1081190
15-2	R	157.4	4.5	5.72E-04	77	37P	671748	1081637
15-3	R	159.6	-13.8	6.19E-04	78	37P	671740	1081575
15-4	R	154.8	-0.6	3.64E-03	80	37P	671704	1081582
15-5	R	168.4	1.1	5.05E-03	82	37P	671633	1081334
15-6	R	189.8	-9.1	1.77E-01	83	37P	671634	1081290
15-8	R	198.0	13.6	1.08E+00	132	37P	671286	1081480
SedSite 16: Dhidinley-Basin N from Mt Galili (W Sector)								
16-1	N	340.6	69.1	1.08E-04	84	37P	669616	1082256
16-2	R	206.6	12.3	6.64E-04	85	37P	669551	1082254
16-3	N	359.5	28.8	9.73E-03	86	37P	669488	1082208
16-6	N	341.2	13.0	8.05E-04	87	37P	669482	1082228
16-7	N	355.2	8.6	6.13E-03	104	37P	669438	1082205
16-9	N	349.1	-52.6	1.70E-03	106	37P	669388	1082189
16-10	N	343.0	7.1	5.41E-04	107	37P	669360	1082189
SedSite 17: Las Danan Area (SE Sector)								
17-1	R	178.3	-23.1	5.07E-04	88	37P	671901	1077434
17-3	N	348.3	18.4	2.16E-03	89	37P	671574	1077257
17-4	N	0.6	19.9	2.39E-02	90	37P	671502	1077270
17-5	N	347.9	22.5	4.64E-02	91	37P	671469	1077233
17-6	N	335.5	23.8	1.34E-01	112	37P	671553	1077972
17-7	N	349.4	35.0	4.73E-03	115	37P	671462	1077227
17-8	R	144.3	-2.4	5.68E-02	116	37P	671439	1077228
17-9	R	202.9	-7.7	3.52E-02	117	37P	671428	1077234
17-10	N	10.7	30.2	4.02E-03	118	37P	671413	1077230
17-11	N	355.2	20.8	3.66E-02	133	37P	671509	1076741
17-12	N	8.3	17.9	3.97E-02	134	37P	671459	1076766
SedSite 18: Area south from Mt.Galili - Lower Shabeley Laag Mb. (W Sector)								
18-1	N	353.4	24.4	1.46E-03	92	37P	669547	1078524
18-2	N	7.9	24.7	1.67E-02	94	37P	669742	1078614
18-3	R	148.9	-19.4	1.18E-02	95	37P	669528	1079052
18-4	R	144.2	-18.9	6.77E-03	96	37P	669523	1079061
18-5	R	170.1	-23.5	6.11E-04	108	37P	669571	1079785
18-7	R	135.7	-25.4	2.88E-04	110	37P	669568	1079747
18-8	R	145.0	0.8	5.75E-04	142	37P	669520	1080024
18-9	R	127.9	-25.8	4.50E-04	143	37P	669501	1080028
18-10	R	166.7	-19.2	1.12E-03	144	37P	669681	1079727
SedSite 19: Area W from Mt.Galili (W Sector)								
19-1	R	164.0	34.9	1.46E-03	97	37P	669230	1080215
19-3	R	176.3	-1.5	5.49E-03	98	37P	669259	1080253
19-4	R	164.7	-10.2	2.17E-02	140	37P	668901	1080472
19-5	R	159.1	-17.9	3.59E-03	141	37P	668829	1080459
SedSite 20: Godiray Valley, Shabeley Laag Mb (W Sector)								
20-4	R	165.9	-14.8	8.19E-02	103	37P	668739	1079663
20-6	R	172.1	-29.4	3.78E-03	102	37P	668746	1079670
SedSite 21: Dhagax Mb (W Sector)								
21-2	N	354.9	20.6	2.17E-03	137	37P	667343	1080253
21-7	R	162.1	-20.9	3.99E-01	139	37P	667408	1080040

placements after the remanence acquisition.

Twelve distinct polarity intervals could be identified by the distribution of normal and reverse characteristic remanence directions from both, volcanic layers and fine-grained sediments (Fig. 8: d,e and Tab. 3). Their correlation with the GPTS of Cande and Kent (1995) is indicated by the age of tuff horizons intercalated with the MGF's volcano-sedimentary pile (Fig. 8: c and Tab. 1). Further magnetostratigraphic subdivision resulted from polarities of primary magnetic vectors identified in volcanic marker horizons and sedimentary deposits in between (Tab. 2 and 3). The combined results from different localities yielded a composite magnetostratigraphic profile comprising the entire MGF (Fig. 8).

5.2 Tectonic interpretation

From an supraregional point of view, the studied Mt.Galili area is sandwiched between the Quaternary Angele and Addo-Do magmatic segments, which display right-stepping lateral off-set tectonics (Fig. 1), related to a distinct NE-migration of the Afar triple junction and a progressive change of plate extension directions throughout the Pliocene (Wolfenden et al., 2004, Kidane et al., 2006). Resultant change of strain field orientation generated re-orientation of hitherto existent fault systems. Thus, newly formed strain fields of internal faults (Wonji fault system) interacted with strain fields of previous marginal fault systems, thereby generating tectonically rhomb-shaped crustal blocks which experienced counterclockwise rotational movement as a result of continued change in strain field orientation. In this regard, Corti et al., (2013) postulate a



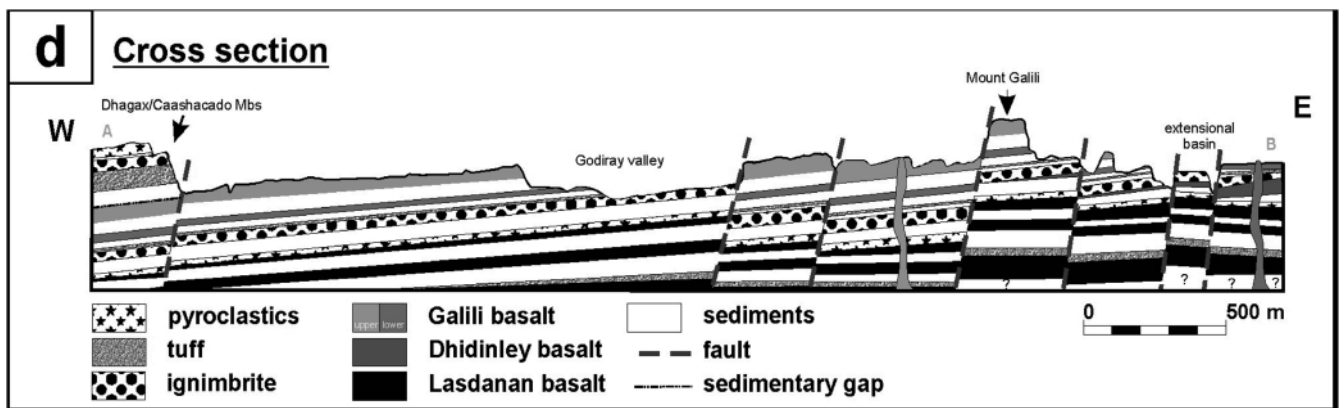


Figure 7: Paleomagnetic directions and implications on the tectonic interpretation of the Mount Galili area: a.) Map showing the relative movement of paleomagnetic vectors with respect to the paleo-geographic reference direction. All vectors (each labelled with a sample site number) are transposed to normal polarity. For each site, the absolute amount of the deviation of observed declination and inclination values (after tilt correction) from the expected paleo-declination and -inclination is demonstrated in Table 2. The Pliocene reference direction for the study area ($183^{\circ}/-13^{\circ}$), calculated from the polar wander path of Besse and Courtillot (2003), is plotted in the map for comparison. (AAZ) arcuate accommodation zone with respect to the migration of the Afar triple junction since ca. 4 Ma (Wolfenden et al., 2004; see Fig. 1). Four different tectonic units can be distinguished based on the paleomagnetic results: (1) Western part of the study area (Mt. Galili area sensu stricto), is characterised by a moderate counterclockwise rotation of the paleomagnetic vectors, (2) Eastern part of the study area (Lasdanan) with virtually unrotated vector directions, (3) a slightly clockwise rotated Ringstructure area, separated by an arcuate accommodation zone (AAZ) from the (4) Satakawini area (N-NE extended research area) with strong counterclockwise rotation. b.+ c.) Site mean directions with α_{95} confidence after tilt correction. Lambert azimuthal equal-area projection displayed with full symbols for lower hemisphere and open symbols for upper hemisphere. For the tectonic interpretation, plots from different areas are combined: (1) Plots for the Mt. Galili area sensu stricto (b), featuring a unique counterclockwise rotation component of 12° (mean value). (2) Plots for the NE extended research area (c), featuring a major counterclockwise rotation of 41° and 52° , respectively (Satakawini) on the one hand and a clockwise mean rotation of 12° (Northern basalt, arcuate accommodation zone) on the other hand. Site locations with divergent mean directions are indicated. d.) Schematic cross section of the Mt. Galili Area (modified after W. Hujer and Ch. Urbanek). Course of the cross section (A-B) is shown in paragraph (a).

transfer zone with dominant strike-slip displacement and block rotations in rift areas amongst Quaternary magmatic segments. As Pliocene to Lower Pleistocene deposits of the Mt. Galili area have been strongly affected by re-orientated strain of the Quaternary Wonji fault system, consequential tectonic features are dominant, apparently forming a new rift structure within the MER.

Areas with different tectonic evolution can be distinguished by the deviation of the mean paleomagnetic vectors from the expected Pliocene reference direction of $183^{\circ}/-13^{\circ}$ (Besse and Courtillot, 2003) in the Mt. Galili survey area (Fig. 7a):

1. The easternmost part of the Mt. Galili area (Lasdanan) exhibits an almost unchanged orientation of the characteristic remanence directions, what we interpret to represent a stable, non-rotated marginal segment of the internal (Wonji) rift zone. In a westward direction, the stable rift segment is bounded by a tectonic zone of sinistral strike-slip displacement features, which, combined with extension (transtension), created counterclockwise block rotations (Fig. 7a,b) that are characteristic features of this marginal transfer zone among ambient Quaternary magmatic segments (Fig. 1).
2. The northern part of the Mt. Galili area (centred by a rhyolitic ring structure) suffered clockwise rotational tilting (up to 12° rotation and up to 19° tilting). This area is considered as a tectonically weakened zone of accommodation between crustal segments (with respect to the migration of the Afar triple junction over the last ca. 4 Ma) and is characterized by slightly clockwise internal block rotations (Fig. 7 a, c) and higher dextral displacement features.

3. In contrast, the western part of the Mt. Galili area (Mt. Galili area sensu stricto) embrace a unique counterclockwise rotation component of 12° (mean value), but the modulus of vector inclination concerning individual rift blocks is variable in either direction (Fig. 7 a, b). Generally, the Mt. Galili area sensu stricto is dominated by steep inclined dip-slip faults, bordering westerly dipping crustal segments.

4. The Satakawini area in the NE extended research region presumably sustained the largest counterclockwise rotation (-36° and -52° rotation) within the investigation area (Fig. 7 a, c), but due to the low number of samples and possible influence of secular variation, we are not sure if these data could be verified sufficiently; further investigations are required. Our findings would infer, that the Satakawini area is displaced relative to the Mt. Galili area sensu stricto by dextral shifting dislocation of crustal segments along an arcuate accommodation zone (AAZ in Fig. 1 and 7a).

We consider the tectonic movements demonstrated in Figure 7 to be the primary result of major block-rotation and tilting following extensional accommodation of crustal segments during the Quaternary (lateral off-set of the Angele and Addo-Do magmatic segments, see Fig. 1) within the northern MER. Generally, the horizontal rotations around a vertical axis are due to the overall rift orientation, not being perpendicular to the plate movements (Casey et al., 2006). Thus, fault bounded blocks are rotated to take up the specific extensional strain in a process known as transtension. Furthermore, concerning mainly the western part of the Mt. Galili area, significant extensional strain caused the overall crustal

block tilting towards the westward situated centre of the (Wonji) rift.

5.3 Stratigraphic implications

The paleomagnetic investigations presented here were focussed on the stratigraphic correlation (Fig. 8) of volcano-sedimentary strata exposed in the Mt. Galili research area (Fig. 2). A composite lithologic profile of the MGF (Fig. 8: a, b, modified after Urbanek et al., 2005 and Hujer et al., 2015), completed with absolute age data from tuff horizons (Fig. 8: c; see Hujer et al., 2015), was the basis for our consideration relating to its magneto-stratigraphic correlation (Fig. 8: f, g, h). Volcanic layers (Fig. 8: d), serving as stratigraphic marker horizons, provided statistically significant magnetic polarity data.

Several successions of sedimentary layers, altogether spanning the entire composite profile of the MGF (Fig. 8: e), were analysed for characteristic remanence directions to determine their magnetic polarity (Tab. 3). Paleomagnetic and radiometric data (Tab.1), as well as lithologic and tectonic field observations were correlated with the composite lithologic profile of the MGF. Finally, a total of 12 polarity zones could be identified (Fig. 8: f) which were assigned to magnetic chrons of the GPTS of Cande and Kent (1995), thus providing a time frame for the deposition of the MGF in the research area (Fig. 8: g, h).

Due to paleomagnetic and radiometric data, a sedimentary gap of ca. 500 ka is supposed between the uppermost Shabeley Laag Member strata (upper Galili basalt) and the Dhagax Member. In this regard, we consider a close connection with extensional rift tectonics occurring simultaneously with basalt magma intrusion and the thereby provoked elevation of ambient rift segments. Consequently, the western area was presumably a morphological high after the upper Galili basalt extrusion, for which reason sedimentation suspended during a substantial time interval. This tectono-magmatic evolutionary trend was already initiated by the extrusion of the lower Galili basalt flow (Lower Shabeley Laag Member). Subsequently, localized rift-block elevation generated lakeside environments, where sometimes windblown costal dunes settled, preferential in the wind shadow of fissure basalt ridges (SE sector, Lasdanan area). Continued tectonic reconfiguration of the scenery is evidenced through a regional, unconformable layering of the upper Galili basalt flow. We consider the highly elevated Mt.Galili rift-block (Fig. 7 d) related to its nearby position to the volcanic feeder channel area of the upper Galili basalt lava extrusion.

5.3.1 Geochronologic arguments

Based on $^{40}\text{Ar}/^{39}\text{Ar}$ data (Tab. 1) provided from Hujer et al. (2015), four different samples (U11, 09/16A, 09/29, 09/32), albeit of different quality, seem to point towards a depositional age around 3.9 Ma. One sample is substantially younger (U51 at 2.35 Ma) and three samples are older (09/16 at ~4.25 Ma, W78 at ~4.43 Ma and W133/2 at ~5.37 Ma). These results are consistent with our stratigraphic field observations, revealing

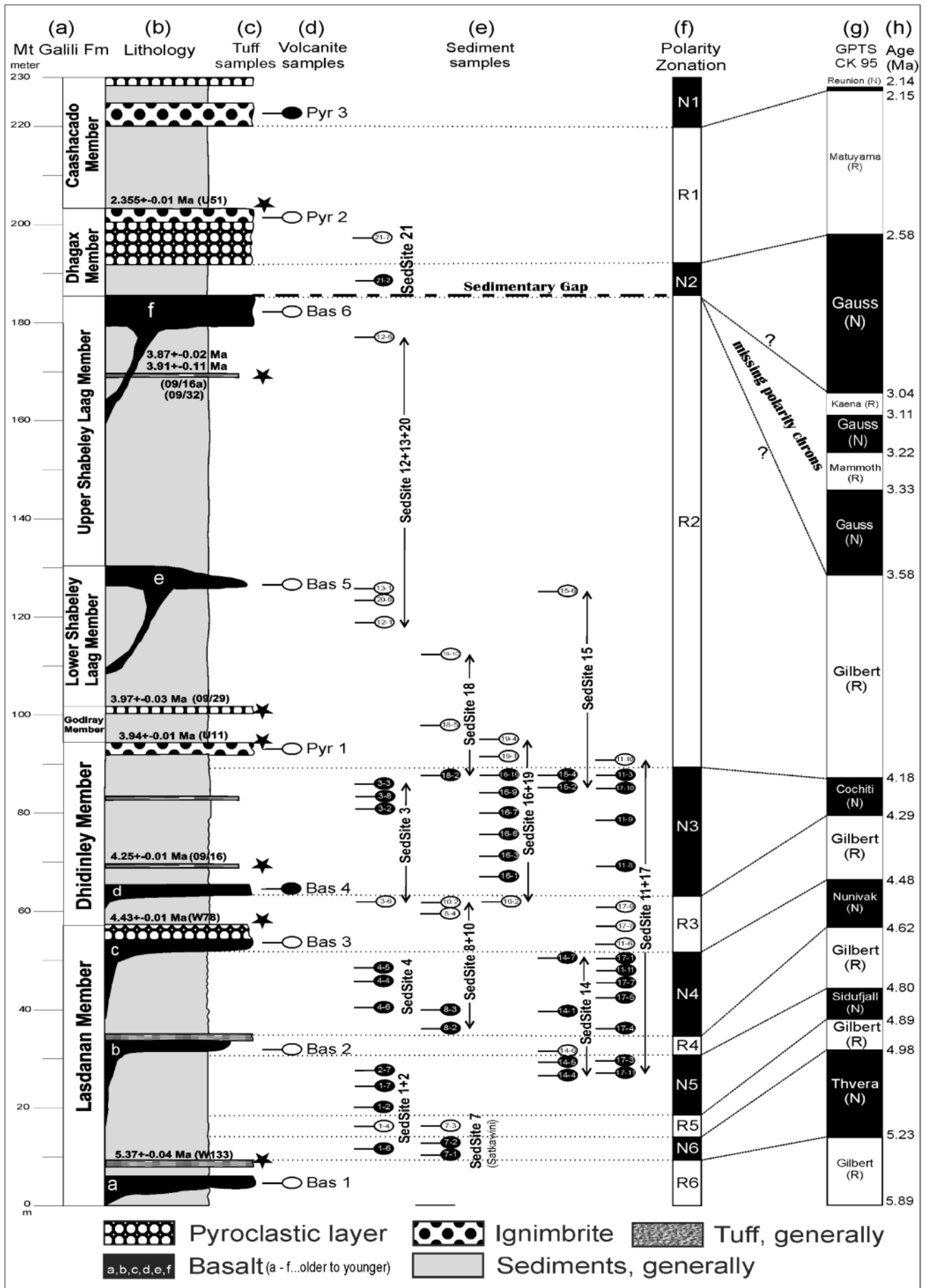
that several ash fall tuff layers cluster around the deposition of a dominant ignimbrite layer in the upper Dhidinley and Godiray members (Fig. 8: d, Pyr 1), marking a time interval around 3.9 Ma. The MGF's basal Lasdanan Member was strongly affected by several eruptions of volcanic fissure basalt lava flows (Fig. 8: d, Bas 1-3), each genetically related with air fall tuff deposition, providing stratigraphic partitioning of different layers and finally marking the very base of the MGF at ca. 5.37 Ma. Furthermore, the substantially younger age at ca. 2.35 Ma provides, combined with magneto-stratigraphic considerations, a strong argument for the existence of a ca. 540 ka lasting gap on top of the Shabeley Laag Member related to suspended sediment accumulation, hence indicating the lack of four magnetic polarity intervals (Fig. 8: g, h).

5.3.2 Magneto-stratigraphic arguments

A tuff sample embedded with sediments of the basal Lasdanan Member indicates an absolute age of 5.37 Ma (Tab.1 / sample W133/2). This volcano-sedimentary pile rests paraconformably on basalt lava flows, which we assign as the very base of the Lasdanan Member. Thus, the MGF's lower limit in the Mt.Galili research area is marked by a massive basement layer of melaphyre-basalt which extruded most probably during the C3r Gilbert (R6 in Fig. 8: f) reverse chron. In the extended SE sector (Satkawini) a fissure basalt extrusion, holding reverse magnetic polarity (Bas 1 in Fig. 8: d) is correlated with this basal layer of the MGF. $^{40}\text{Ar}/^{39}\text{Ar}$ dating of a surge layer at the base of the Dhidinley Member provides an upper age boundary of 4.43 Ma (Tab.1: sample W78) for the Lasdanan Member. Our paleomagnetic investigations yielded seven successive polarity zones within the Lasdanan Member, comprising a time range from ca 5.37 to 4.43 Ma, which we assign to the C3r Gilbert (R6), C3n.4n Thvera (N6), C3n.3r Gilbert (R5), C3n.3n Sidufjall (N5), C3n.2r Gilbert (R4), C3n.2n Nunivak (N4) and C3n.1r Gilbert (R3) chrons (Fig. 8: f, g).

Based on $^{40}\text{Ar}/^{39}\text{Ar}$ data (Tab. 1), the Dhidinley Member spans the time interval from ca.4.43 to 3.92 Ma. Deposits of this member yield a succession of three polarity zones, comprising the C3n.1r Gilbert (R3) reverse chron, the C3n.1n Cochiti

Figure 8: Magneto-stratigraphy of the MGF as reported here. Column (a) shows the stratification and thickness of the MGF. Column (b) is a generalized lithologic profile with a simplified display of sediment portions modified after Urbanek et al. (2005). Column (c) indicates the position (★) of tuffs and ignimbrites used for absolute $^{40}\text{Ar}/^{39}\text{Ar}$ dating of feldspar minerals as presented in Hujer et al. (2015), resultant absolute age data with their related sample number (Tab. 1) are indicated. Column (d) marks the position and magnetic polarity of volcanic rock layers (Bas=Basalt, Pyr=Pyroclastics), which were sampled as drill cores at different locations in the research area (Drill Sites*). Column (e) indicates the stratigraphic range and magnetic polarity of sediments (cube samples) from selected profiles (Sed Site*). Column (f) gives the polarity zonation suggested here. Column (g) depicts part of the GPTS of Cande and Kent (1995) and tie lines to column (f) denote probable correlations, assuming that four polarity subchrons are missing due to a sedimentary gap in the time interval from 3.04 to 3.58 Ma. Column (h) gives ages of magnetic polarity transitions as accepted by Cande and Kent (1995). * Details are given in Tab. 2 and 3.



(N3) normal chron and parts of the C2Ar Gilbert (R2) reverse chron (Fig. 8: f, g). Godiray and Shabeley Laag members show continuous reverse polarity, which is assigned to the C2Ar Gilbert (R2) chron (Fig. 8: f, g) indicating a time range between ca 3.92 Ma and ca. 3.58 Ma.

Red ignimbrites of the Dhagax Member are dated to 2.33 Ma (Tab.1: sample U51), thus their reverse polarity zone is assigned to the C2r.2r Matuyama (R1) chron (Fig. 8: f, g). Underlying coarse grained sediments probably represent the C2.An.1n Gauss (N2) chron. Hence, we propose a lack of four polarity intervals due to the formation of an erosional surface linked to the extensive basalt lava flow (upper Galili basalt) in the upper Shabeley Laag Member. The top of the Caashacado Member is marked by a normal polarity zone, which is attributed to the C2r.1n Reunion (N1) normal chron (Fig. 8: f, g), indicating an upper limit of ca. 2.15 Ma for the hitherto existing range of the MGF.

6. Conclusions

Based on our radiometric and paleomagnetic results, the volcano-sedimentary strata of the Mount Galili Formation (MGF) were deposited between ca. 5.37 and ca. 2.15 Ma. The lower four members of the MGF (Lasdanan, Dhidinley, Godiray and Shabeley Laag) cover nine magnetic polarity intervals within a time span of 5.37 to 3.58 Ma for their deposition. Consequently, they can be chronologically correlated with the Sagantole Formation in Northern Ethiopia (Renne et al., 1999; Quade et al., 2008).

The upper two members of the MGF (Dhagax and Caashacado) contain three polarity intervals (chrons C2An.1n [N2], C2r.2r [R1] and C2r.1n [N1]) ordered around an Ar/Ar age of ca. 2.35 Ma, thereby providing the formations upper age limit of ca. 2.15 Ma. Thus, we conclude that, with respect to the GPTS of Cande and Kent (1995), four polarity intervals (chrons C2An.3n, C2An.2r, C2An.2n and C2An.1r) and consequently ca 540 ka, from 3.58 to 3.04 Ma, are missing within the succession, between the lower and upper MGF.

We assign this significant depositional gap to tectonic uplift processes of the region caused by the eruption of the upper Galili basalt lavas during deposition of the Upper Shabeley Laag Member. Hence, isochronic deposits of the Hadar Formation, which accumulated elsewhere between ca. 3.8 to 2.9 Ma, do not exist in the Mt.Galili study area. Instead, a major, area-wide, angular unconformity separates the upper Galili basalt layer (top of lower MGF) from overlying lacustrine and conglomeratic fluvial channel deposits as well as pumice tuff, ignimbrite and pyroclastics of the upper MGF (Dhagax- and Caashacado Members), which may be correlated with the Busidima Formation elsewhere (Quade et al., 2008). Thus, their accumulation may be related to major tectonic faulting and crustal subsidence since ca. 2.9 Ma as well as to pyroclastic eruptions around 2.4 Ma resulting from recurrent faulting (Tiercelin, 1986).

Furthermore, our paleomagnetic vector data from volcanic layers indicate that the research area was subjected to rift-re-

lated tectonics (crustal block rotation and tilting) relative to the stable African crust since the Pliocene. We consider the Mt.Galili area to be a central segment of the northern MER, where extensional rift-tectonics evolved since the Miocene, thereby affecting the Pliocene to early Pleistocene stratification of the MGF permanently. Since the Quaternary, the Mt. Galili area was sandwiched between newly formed magmatic segments, which display characteristic right-stepping lateral off-set tectonics. This tectonic setting may be induced by an arcuate accommodation zone with respect to the migration of the Afar triple junction for the last 4 Ma (Wolfenden et al., 2004), but the major impact happened in the Quaternary period, when the generation of weakened zones within a progressively thinned crust triggered re-orientation of a newly formed internal fault system (Wonji Fault System) with respect to the trend of the pre-existing Miocene border fault system of the northern MER (Bonini et al., 2005; Corti, 2009). Thus, faults of two trends interacted within an oblique strain field relative to the divergence directions of the Nubian- and Somalian plates, finally resulting in rhomb-shaped tectonic patterns with both, dip-slip and strike-slip displacement. Minor counter-clockwise block rotations are required to accommodate the difference in slip direction along the different fault systems (Corti et al., 2013). This is supported by our paleomagnetic data. Due to the intermittent position of the Mt.Galili area between the Angele and Addo-Do magmatic segments, a transfer zone, with dominant strike-slip displacement, triggered significant tectonic structures such as strike-slip extensional basins in the eastern sectors of the research area. Supposedly, due to closeness of the Mt. Galili region towards the Afar triple-junction, the dimensions of tectonic dislocations are appreciably higher than those observed in central regions of the MER (Kidane et al., 2009).

Acknowledgements

This work was supported by the Austrian Science Fund project (no. P15196-B06, leader P. Faupl) "Riftsedimentation und Vulkanismus in der Afar Senke/Äthiopien", sponsoring the geological investigations in the years 2001 – 2004, as well as the Austrian Council for Science and Technology, project (200.093/3-VI/1/04) and the Austrian Federal Ministry for Science and Research, project (AD 387/25-30), the latter in cooperation with the Institute of Anthropology of the University of Vienna. A sincere thank you to Wolfgang Hujer (Vienna) and Klaudia Kuiper (Amsterdam), who provided lithostratigraphic and absolute age data. We are grateful to Horst Seidler, Katrin Schäfer and Gerhard Weber as well as to Bence Viola, Ottmar Kullmer and Andrea Stadlmayr for providing support with field work organization and scientific teamwork. Peter Faupl and an anonymous reviewers are highly acknowledged for their very constructive reviews and valuable suggestions.

References

- Audin, L., X. Quidelleur, E. Coulié, V. Courtillot, S. Gilder, I. Manighetti, P.Y. Gillot, P. Tapponnier, and T. Kidane (2004), Paleomagnetism and K-Ar and $^{40}\text{Ar}/^{39}\text{Ar}$ ages in the Ali-Sabieh area (Republic of Djibouti, and Ethiopia): Constraints on the mechanism of Aden ridge propagation into Southeastern Afar during the last 10 Myr, *Geophysical Journal International*, 158, 327–345, doi:10.1111/j.1365-246X.2004.02286.x.
- Ayalew, D., Ebinger, C., Bourdon, E., Wolfenden, E., Yirgu, G., and Grassineau, N., 2006. Temporal compositional variation of early syn-rift rhyolites along the western Red Sea margin and northern Main Ethiopian rift. In: G. Yirgu, C.J. Ebinger, and P.K.H. Maguire (eds.), *The Afar Volcanic Province within the East African Rift System*. Geological Society of London Special Publication, 259, pp. 121–130. <https://doi.org/10.1144/GSL.SP.2006.259.01.10>
- Barberi, F. and Varet, J., 1975. Recent volcanic units of Afar and their structural significance. In: A. Pilger and A. Rosler (eds.), *Afar depression of Ethiopia*, Proceedings of an international symposium on the Afar region and rift related problems, Bad Bergzabren, Germany, 1974: Vol. 1, E. Schweizerbart'sche Verlagsbuchhandlung, Stuttgart, Germany (1975), pp. 174–178.
- Barberi, F. and Varet, J., 1977. Volcanism in Afar: small-scale plate tectonic implications. *Bulletin of the Geological Society of America*, 88, 1251–1266.
- Besse, J. and Courtillot, V., 2003. Apparent and true polar wander and the geometry of the geomagnetic field in the last 200 million years. *Journal of Geophysical Research*, 107/B11, 2156–2202.
- Beyene, A. and Abdelsalam, M., 2005. Tectonics of the Afar Depression: A review and synthesis. *Journal of African Earth Sciences*, 41, 41–59. <https://doi.org/10.1016/j.jafrearsci.2005.03.003>
- Bonini, M., Corti, G., Innocenti, F., Manetti, P., Mazzarini, F., Abebe, T. and Pecskey, Z., 2005. Evolution of the Main Ethiopian Rift in the frame of Afar and Kenya rifts propagation. *Tectonics*, 24/1. doi:10.1029/2004TC001680. <https://doi.org/10.1029/2004TC001680>
- Buck, W.R., 2006. The role of magma in the development of the Afro-Arabian Rift System. In: G. Yirgu, C.J. Ebinger, and P.K.H. Maguire (eds.), *The Afar Volcanic Province within the East African Rift System*. Geological Society of London, Special Publication, 259, pp. 43–54. <https://doi.org/10.1144/GSL.SP.2006.259.01.05>
- Cande, S.C. and Kent, D.V., 1995. Revised calibration of the geomagnetic polarity time scale for the Late Cretaceous and Cenozoic. *Journal of Geophysical Research*, 100, 6093–6095. <https://doi.org/10.1029/94JB03098>
- Casey, M., Ebinger, C., Keir, D., Gloaguen, R., Mohammed, F., 2006. Strain accommodation in transitional rifts: extension by magma intrusion and faulting in Ethiopian rift magmatic segments. In: G. Yirgu, C.J. Ebinger, and P.K.H. Maguire (eds.), *The Afar Volcanic Province within the East African Rift System*. Geological Society of London, Special Publication, 259, pp. 143–163. <https://doi.org/10.1144/GSL.SP.2006.259.01.13>
- Chadima, M., Hrouda, F., 2006. Remasoft 3.0: a user-friendly paleomagnetic data browser and analyzer. *Travaux Géophysiques*, 27, 20–21.
- Corti, G., 2009. Continental rift evolution: from rift initiation to incipient break-up in the Main Ethiopian Rift. *East African Earth Science Reviews*, 96, 1–53.
- Corti, G., Philippon, M., Sani, F., Keir, D. and Kidane, T., 2013. Re-orientation of the extension direction and pure extensional faulting at oblique rift margins: comparison between the Main Ethiopian Rift and laboratory experiments. *Terra Nova*, 25/5, 396–404. <https://doi.org/10.1111/ter.12049>
- Dupont-Nivet, G., Sier, M., Campisano, C.J., Arrowsmith, J.R., DiMaggio, E., Reed, K., Lockwood, C., Franke, C. and Hüsing, S., 2008. Magnetostratigraphy of the eastern Hadar Basin (Ledi-Geraru research area, Ethiopia) and implications for hominin paleoenvironments. In: J. Quade and J.G. Wynn (eds), *The Geology of Early Humans in the Horn of Africa*. Geological Society of America, Special Papers, 446, pp. 67–85.
- Ebinger, C.J. and Casey, M., 2001. Continental breakup in magmatic provinces: an Ethiopian example. *Geology*, 29, 527–530.
- Haile-Selassie, Y., Gilbert, L., Melillo, S.T. M., Ryan, T. M., Alene, M., Deino, A., Levon, N. E., Scott, G. and Saylor, B. Z., 2015. New species from Ethiopia further expands Middle Pliocene hominin diversity. *Nature*, 521, 483–488. <http://dx.doi.org/10.1038/nature14448>
- Hayward, N. J., and Ebinger, C.J., 1996. Variations in the long-axis segmentation of the Afar rift system. *Tectonics*, 15, 244–257. <https://doi.org/10.1029/95TC02292>
- Hendrie, D.B., Kuszniir, N.J., Morley, C.K. and Ebinger, C.J., 1994. Cenozoic extension in northern Kenya: a quantitative model of rift basin development in the Turkana region. *Tectonophysics*, 236, 409–438.
- Hujer, W., Kuiper, K., Bence, V., Wagreich, M. and Faupl, P., 2015. Lithostratigraphy of the late Miocene to Early Pleistocene, hominide-bearing Galili Formation, Southern Afar Depression, Ethiopia. *Austrian Journal of Earth Sciences*, 108/2, 105–127. <https://doi.org/10.17738/ajes.2015.0016>
- Keir, D., Ebinger, C.J., Stuart, G.W., Daly, E. and Ayele, A., 2006. Strain accommodation by magmatism and faulting as rifting proceeds to breakup: Seismicity of the northern Ethiopian rift. *Journal of Geophysical Research*, 111/B5. <https://doi.org/10.1029/2005JB003748>
- Kidane, T., Platzman, E., Ebinger, C., Abebe, B. and Rochette, P., 2006. Paleomagnetic constraints on Continental break-up processes: observations from the Main Ethiopian rift. In: G. Yirgu, C.J. Ebinger, and P.K.H. Maguire (eds.), *The Afar Volcanic Province within the East African Rift System*. Geological Society of London, Special Publication, 259, pp. 165–183. <https://doi.org/10.1144/GSL.SP.2006.259.01.14>
- Kidane, T., Otofujii, Y.I., Komatsu, Y., Shibasaki, H. and Rowland, J., 2009. Paleomagnetism of the Fentale-magmatic segment, main Ethiopian Rift: New evidence for counterclockwise block rotation linked to transtensional deformation. *Physics of the Earth and Planetary Interiors*, 176, 109–123.

- Kidane, T., Brown, F.H. and Kidney, C., 2014. Magnetostratigraphy of the Fossil-rich Shungura Formation, southwest Ethiopia. *Journal of African Earth Sciences*, 97, 207–223.
- Kimbel, W. H. & Deleuzene, L. K., 2009. 'Lucy' redux: a review of research on *Australopithecus afarensis*. *American Journal of Physical Anthropology* 49, 2–48 (2009).
- Kullmer, O., Sandrock, O., Viola, B., Hujer, W., Said, H., and Seidler, H., 2008. Suids, Elephantoids and Paleoecology of the Pliocene Galili Hominid Site, Somali Region, Ethiopia. *Palaios*, 23, 452-464. <http://dx.doi.org/10.2110/palo.2007.p07-028r>
- Macchiarelli, R., Bondioli, L., Falk, D., Faupl, P., Illerhaus, B., Kullmer, O., Richter, W., Said, H., Sandrock, O., Schafer, K., Urbanek, C., Viola, B.T., Weber, G.W. and Seidler, H., 2004. Early Pliocene hominid tooth from Galili, Somali Region, Ethiopia. *Collegium Antropologicum*, 28, Supplement 2, 65-76.
- Manighetti, I., Tapponnier, P., Gillot, P.Y., Jacques, E., Courtillot, V., Armijo, R., Ruegg, J.C. and King, G., 1998. Propagation of rifting along the Arabia-Somalia plate boundary: Into Afar. *Journal of Geophysical Research*, 103, 4947-4974.
- Pizzi, A., Coltorti, M., Abebe, B., Disperati, L., Sacchi, G. and Salvini, R., 2006. The Wonji Fault Belt (Main Ethiopian Rift, Ethiopia): Structural and geomorphological constraints and GPS monitoring, In: G. Yirgu, C.J. Ebinger, and P.K.H. Maguire (eds.), *The Afar Volcanic Province within the East African Rift System*. Geological Society of London, Special Publication, 259, pp. 191-208. <https://doi.org/10.1144/GSL.SP.2006.259.01.16>
- Quade, J., Levin, N.E., Simpson, S.W., Butler, R., McIntosh, W.C., Semaw, S., Kleinsasser, L., Dupont-Nivet, G., Renne, P., and Dunbar, N., 2008. The geology of Gona, Afar, Ethiopia. In: J. Quade and J.G. Wynn (eds), *The Geology of Early Humans in the Horn of Africa*. Geological Society of America, Special Papers, 446, pp. 1–31.
- Renne, P.R., Wolde Gabriel, G., Hart, W.K., Heiken, G. and White, T.D., 1999. Chronostratigraphy of the Miocene-Pliocene Sagentole Formation, Middle Awash Valley, Afar rift, Ethiopia. *Geological Society of America Bulletin*, 111/6, 869-885.
- Ring, U., 2014. The East African Rift System. *Austrian Journal of Earth Sciences*, 107/1, 132-146.
- Tesfaye, S., Kusky, T.T. and Harding, D., 2003. Early Continental breakup boundary and migration of the Afar triple junction, Ethiopia. *Bulletin of the Geological Society of America*, 115, 1053–1067.
- Tesfaye, S., Rowan, M.G., Mueller, K., Trudgill, B.D. and Harding, D.J., 2008. Relay and accommodation zones in the Dobe and Hanle grabens, central Afar, Ethiopia and Djibouti. *Journal of the Geological Society of London*, 165/2, 535-547.
- Thébaud, E., Finlay, Ch., Beggan, C., Alken, P., Aubert, J., Barrois, O., Bertrand, F., Bondar, T., Boness, A., Brocco, L., Canet, E., Chambodut, A., Chulliat, A., Coisson, P., Civet, F., Du, A., Fournier, A., Fratter, I., Gillet, N., Hamilton, B., Hamoudi, M., Hulot, G., Jager, Th., Korte, M., Kuang, W., Lalanne, X., Langlais, B., Léger, J.M., Lesur, V., Lowes F.J., et al., 2015. International Geomagnetic Reference Field: the 12th generation. *Earth, Planets and Space* 2015, 67-79.
- Tiercelin, J.J., 1986. The Pliocene Hadar Formation, Afar depression of Ethiopia. In: Frostick, L.E., Renaut, R.W., Reid, I. and Tiercelin, J.J. (eds), *Sedimentation in the African Rifts*. Geological Society of London Special Publications, 25, pp. 221-40.
- Urbanek, Ch., Faupl, P., Hujer, W., Ntaflos, T., Richter, W., Weber, G., Schaefer, K., Viola, B., Gunz, P., Neubauer, S., Stadlmayr, A., Kullmer, O., Sandrock, O., Nagel, D., Conroy, G., Falk, D., Woldearegay, K., Said, H., Assefa, G., and Seidler, H., 2005. *Geology, Paleontology and Paleoanthropology of the Mount Galili Formation in the southern Afar Depression, Ethiopia – Preliminary results*. *Joannea Geologie und Paläontologie*, Graz, 6, 29-43.
- Varet, J., 1978. *Geology of Central and Southern Afar* (Geological Map 1:500.000). Centre National de la Recherche Scientifique, Paris, pp. 1-124.
- Weber, G.W., Seidler, H., Machiarelli, R., Bondioli, L., Faupl, P., Richter, W., Kullmer, O., Sandrock, O. & Falk, D., 2001. New discovery of *Australopithecus* in the Somali region of Ethiopia. Abstracts of AAPA poster and podium presentations. *American Journal of Physical Anthropology*, 114, S32, p 162, 2001. DOI:10.1002/ajpa.1040
- White T.D., Suwa, G., Hart, W.K., Walter, R.C., WoldeGabriel, G., Heinzelin, J., Clark, J.D., Asfaw, B. & Vrba, E.S., 1993. New discoveries of *Australopithecus* at Maka in Ethiopia. *Nature* 366:261–265.
- White, T. D., WoldeGabriel, G., Asfaw, B., Ambrose, St., Beyene, Y., Bernor, R.L., Boissérie, J-R., Currie, B., Gilbert, H., Haile-Selassie, Y., Hart, W.K., Hlusko, L.J., Howell, F.C., Kono, R.T., Lehmann, Th., Louchart, A., Lovejoy, C.O., Renne, P.R., Saegusa, H., Vrba, E.S., Wesselman, H. & Suwa, G., 2006. Asa Issie, Aramis and the origin of *Australopithecus*. *Nature* 440, 883–889 (2006).
- White, T. D., Asfaw, B., Beyene, Y., Haile-Selassie, Y., Lovejoy, C.O., Suwa, G., WoldeGabriel, G., 2009. *Ardipithecus ramidus* and the Paleobiology of Early Hominids. *Science* 326, 64 (2009); DOI:10.1126/science.1175802
- Wolfenden E., Ebinger C., Yirgu G., Deino A. and Ayalew D., 2004. Evolution of the northern Main Ethiopian rift: birth of a triple junction. *Earth and Planetary Science Letters*, 224, 213-228.

Received: 06 November 2017

Accepted: 29 December 2017

Fritz POPP^{1*)} & Robert SCHOLGER²⁾

¹⁾ Department of Geodynamics and Sedimentology, University of Vienna, Althanstrasse 14, 1090 Vienna, Austria;

²⁾ Chair of Applied Geophysics, Montanuniversität Leoben, Peter Tunner Str. 25, 8700 Leoben, Austria;

^{*)} Corresponding author, friedrich.popp@univie.ac.at